Received: 29 January 2022 | Revised: 5 October 2022 | Accepted: 9 November 2022

DOI: 10.1002/rnc.6503

RESEARCH ARTICLE

WILEY

Incremental nonlinear dynamic inversion based path-following control for a hybrid quad-plane unmanned aerial vehicle

Li Zhou[1] | **Jingtao Yang**[2] | **Tilman Strampe**[1] | **Uwe Klingauf**[1]

[1]Institute of Flight Systems and Automatic Control, Department of Mechanical Engineering, Technical University of Darmstadt, Darmstadt, Germany

[2]Department of Electrical Engineering and Information Technology, Technical University of Darmstadt, Darmstadt, Germany

Correspondence
Li Zhou, Institute of Flight Systems and Automatic Control, Department of Mechanical Engineering, Technical University of Darmstadt, Darmstadt, Germany.
Email: zhou@fsr.tu-darmstadt.de

Funding information
China Scholarship Council

Abstract

Hybrid quad-plane unmanned aerial vehicles (UAVs), which combine the advantages of multicopters and fixed-wing UAVs, are gaining increasing attention. However, quad-planes are characterized by complex structures, high nonlinearity, strong coupling, and three flight regimes (hover, transition, and fixed-wing flight), which bring great challenges to the research of their control laws. This article aims to design control laws for a quad-plane in fixed-wing and hover flight regimes based on a robust nonlinear control method, incremental nonlinear dynamic inversion (INDI), so that the quad-plane can follow a given path autonomously. Firstly, a mathematical model of the quad-plane is established on the basis of kinematics and dynamics. Subsequently, cascade control structures are proposed and divided into inner and outer loops. A control law is designed for each control loop based on INDI. To improve the performance of the designed control law, reference models are added to the inner loops to shape the input commands and provide feedforward inputs. Finally, simulation results corroborate the performance and robustness of the proposed control law. Compared with the control law designed by active disturbance rejection control and proportional-integral-derivative control methods, the INDI-based control law is more robust.

KEYWORDS

hybrid quad-plane unmanned aerial vehicle, incremental nonlinear dynamic inversion, nonlinear control, path following

1 | INTRODUCTION

In recent years, unmanned aerial vehicles (UAVs) have gained a lot of attention due to the wide range of applications in military and civilian fields such as surveillance, patrol, mapping, and transportation.[1-4] There are two main types of conventional UAVs: multicopters and fixed-wing UAVs. Multicopters stand out for their capability of hovering in the air and having no special requirements for take-off and landing, but they have speed and endurance limitations. On the other hand, fixed-wing UAVs can fly at higher speeds and maintain long-endurance, while they require much space to take off and land and cannot hover in the air. With the growing mission complexity of UAVs, these two types of UAVs are

challenging to meet requirements. Hybrid quad-plane UAVs, also known as dual-system hybrid UAVs, are novel and promising UAVs that combine the benefits of these two types of UAVs without a tilting mechanism. They have two independent propulsion systems: propulsion systems of multicopters and fixed-wing UAVs, so there are three flight regimes: hover, transition, and fixed-wing flight.[5] Due to this type of UAV's ease of design and versatility, they are gaining great research interest.

As quad-planes combine propulsion systems of multicopters and fixed-wing UAVs, their physical configurations are complex, and mathematical models are highly nonlinear. Aerodynamic interactions between the fixed wing and rotors pose a challenge for modeling. When designing control laws, the characteristics of both fixed-wing UAVs and multicopters need to be considered, which adds complexity to the analysis. Meanwhile, most modern UAV missions (e.g., precision agriculture and 3D mapping) require autonomous flights and following a given path. Therefore, designing a control law for the novel quad-plane to autonomously follow a path is significant for the future use of such UAVs in the industry.

Compared with tilt-rotor,[6-8] tilt-wing,[9-11] and tail-sitter[12-14] UAVs, the research on quad-planes is in the initial stage. Çakici et al.[15] designed a quad-plane and analyzed its mathematical model. Flight control laws based on the proportional-integral-derivative (PID) control method were designed for hover and fixed-wing flight regimes. In the work of Dewi and Hadi et al.,[16-18] a quad-plane was constructed, and computational fluid dynamics (CFD) simulations were conducted to analyze its aerodynamics. Then, the avionics system and control scenario were presented. A switching control approach was proposed to maintain a stable transition. Gu et al.[19] developed and tested a quad-plane. A PID controller-based flight control system was designed to achieve autonomous flight. In the work of Zhang and Lin et al.,[20,21] mathematical models and transition control schemes for quad-planes were studied to achieve a stable flight. Hanel et al.[22] did research about a quad-plane that has eight lift motors. The detailed configuration of the quad-plane and control laws based on the PID controller were presented. However, when establishing the mathematical model in these existing works, the fixed-wing and hover flight regimes are studied separately. Then, the forces and moments are added together regardless of their interactions. Most controller design methods are based on the conventional PID control law. The earlier research primarily aims to achieve a successful flight without further research to accomplish more complex missions and improve flight performance.

Meanwhile, incremental nonlinear dynamic inversion[23,24] (INDI) is gaining increasing attention in the field of flight control. As an extension of nonlinear dynamic inversion (NDI),[25] it has better robustness and less dependency on a detailed model of the controlled object. In the work of Veld et al.[26] and Wang et al.,[27] the theoretical studies on INDI, including stability and robustness analyses, were conducted. Smeur et al.[28,29] utilized INDI to design an attitude control law for a micro quadcopter and attitude and position control laws for a tail-sitter UAV. Besides, INDI has also been used to design a control law for a tilt-rotor UAV[30,31] and an unmanned aerial-underwater vehicle.[32] In the work of Lu et al.,[33] a fault-tolerant trajectory control law for an aircraft was studied based on INDI. Karssies[34] proposed an extended incremental nonlinear control allocation method for a quad-plane. In summary, INDI has been utilized in control law design for different aerial vehicles. To the authors' knowledge, there is less related work on designing INDI-based path-following control laws for a quad-plane. Furthermore, active disturbance rejection control[35] (ADRC) is also a robust and easy-to-use control method frequently used in recent research on UAV flight control.[36,37]

Motivated by the above analysis, an INDI-based path-following control law for a quad-plane is proposed in this article to expand the application field of quad-planes, and it is compared with the control law designed based on ADRC and PID control. The hover and fixed-wing flight regimes are considered first, as they are primary flight regimes of quad-planes. The main contributions of this article are summarized as follows:

i. A path-following control law is designed for the fixed-wing flight regime of a quad-plane. INDI, an advanced control method, is utilized to enhance control performance. A cascade control structure is designed first, and then the detailed control law for each loop is elaborated. Simulations are carried out in the presence of wind gust disturbances and model parameter uncertainties to verify the performance and robustness of the control law in the fixed-wing flight regime.
ii. An INDI-based path-following control law for the hover flight regime of the quad-plane is also studied. The control law is proposed based on a cascade control structure. Simulation results demonstrate the quad-plane's good path-following performance and the control law's robustness in the hover flight regime.

The remainder of this article is organized as follows. Section 2 presents the quad-plane's configuration and establishment of the mathematical model. The INDI theory and derivation process are elaborated in Section 3. Section 4 and Section 5 detail the control law design for fixed-wing and hover flight regimes, respectively. Simulation results and corresponding analysis are given in Section 6. Finally, conclusions are drawn in Section 7.

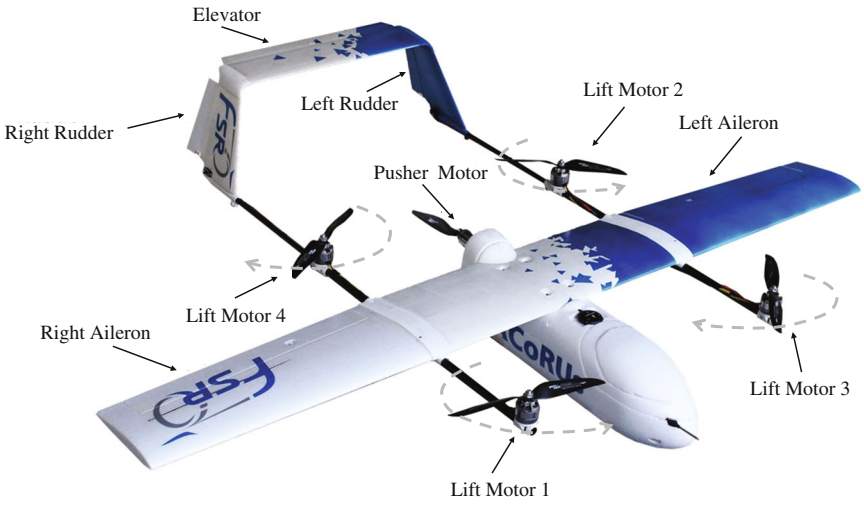

FIGURE 1 Quad-plane configuration

TABLE 1 Basic parameters of the quad-plane

Parameter	Value
Mass m	3.95 kg
Moment of inertia I_{xx}	0.2508 kg · m^2
Moment of inertia I_{yy}	0.2902 kg · m^2
Moment of inertia I_{zz}	0.5055 kg · m^2
Product of inertia I_{xz}	0.0308 kg · m^2
Wing area S	0.41 m^2
Wing span b	1.827 m
Mean aerodynamic chord c	0.23 m
Distance from lift motor to C.G. d_x, d_y	0.32 m
Distance from lift motor to C.G. d_z	0.0872 m
Pusher propeller thrust coefficient C_p	0.07
Pusher propeller diameter D	0.3302 m

2 | QUAD-PLANE DESCRIPTION AND MATHEMATICAL MODEL

2.1 | Quad-plane configuration

The quad-plane platform studied in this article is presented in Figure 1, and the configuration of this quad-plane is self-designed. There are four lift motors for lift, one pusher motor for thrust, and five control surfaces including two ailerons, one elevator, and two rudders. The four lift motors are distributed in a square shape on both sides of the fuselage, while the pusher motor is located along the x-axis in the body frame. The pusher propeller has no inclination angle. Lift motors 1 and 2 rotate counterclockwise, and lift motors 3 and 4 rotate clockwise. Some configuration parameters are listed in Table 1.

2.2 | Mathematical model

The mathematical model of the quad-plane can be expressed as

$$\dot{\boldsymbol{x}} = \boldsymbol{f}(\boldsymbol{x},\ \boldsymbol{u}), \tag{1}$$

where $\boldsymbol{x}$ and $\boldsymbol{u}$ denote state and control variables, respectively. The state variables consist of the position variables (p_n, p_e, p_d) with respect to the inertial frame, the linear velocities (u, v, w) with respect to the body frame, the Euler angles (ϕ, θ, ψ), and the angular velocities (p, q, r) with respect to the body frame.[38] The control variables include the rotational speeds of the four lift motors (ω_1, ω_2, ω_3, ω_4), the rotational speed of the pusher motor ω_p, the left and right aileron deflections (δ_{a_l}, δ_{a_r}), the elevator deflection δ_e, and the left and right rudder deflections (δ_{r_l}, δ_{r_r}).

To derive the mathematical model, the equations of motion are evolved, including kinematic and dynamic equations. The kinematic equations[38] are defined by the coordinate frame transformations as follows:

$$\begin{bmatrix}\dot{p}_n\\ \dot{p}_e\\ \dot{p}_d\end{bmatrix}=\begin{bmatrix}\cos\theta\cos\psi & \sin\phi\sin\theta\cos\psi-\cos\phi\sin\psi & \cos\phi\sin\theta\cos\psi+\sin\phi\sin\psi\\ \cos\theta\sin\psi & \sin\phi\sin\theta\sin\psi+\cos\phi\cos\psi & \cos\phi\sin\theta\sin\psi-\sin\phi\cos\psi\\ -\sin\theta & \sin\phi\cos\theta & \cos\phi\cos\theta\end{bmatrix}\begin{bmatrix}u\\ v\\ w\end{bmatrix}, \tag{2}$$

$$\begin{bmatrix}\dot{\phi}\\ \dot{\theta}\\ \dot{\psi}\end{bmatrix}=\begin{bmatrix}1 & \sin\phi\tan\theta & \cos\phi\tan\theta\\ 0 & \cos\phi & -\sin\phi\\ 0 & \sin\phi/\cos\theta & \cos\phi/\cos\theta\end{bmatrix}\begin{bmatrix}p\\ q\\ r\end{bmatrix}. \tag{3}$$

Referring to Newton's second law, the dynamic equation[38] for the translational motion is

$$\begin{bmatrix}\dot{u}\\ \dot{v}\\ \dot{w}\end{bmatrix}=\begin{bmatrix}rv-qw\\ pw-ru\\ qu-pv\end{bmatrix}+\frac{1}{m}\begin{bmatrix}F_x\\ F_y\\ F_z\end{bmatrix}, \tag{4}$$

where F_x, F_y, and F_z denote the forces along x-, y-, and z-axes in the body frame, respectively. For the rotational motion, the dynamic equation[38] with respect to the balance of moments follows as

$$\begin{bmatrix}\dot{p}\\ \dot{q}\\ \dot{r}\end{bmatrix}=\boldsymbol{I}^{-1}\left(-\begin{bmatrix}p\\ q\\ r\end{bmatrix}\times\left(\boldsymbol{I}\begin{bmatrix}p\\ q\\ r\end{bmatrix}\right)+\begin{bmatrix}M_{\text{roll}}\\ M_{\text{pitch}}\\ M_{\text{yaw}}\end{bmatrix}\right), \tag{5}$$

where $\boldsymbol{I}$ is the moment of inertia matrix, and M_{roll}, M_{pitch}, and M_{yaw} are the moments along x-, y-, and z-axes in the body frame, respectively.

As shown in the dynamic equations, the forces and moments acting on the UAV cause changes in its motion. The gravitational force $\boldsymbol{F}_g$, the force produced by the pusher motor $\boldsymbol{F}_p$, the aerodynamic force $\boldsymbol{F}_a$, and the force produced by lift motors $\boldsymbol{F}_l$ are the main components of the total force $\boldsymbol{F}_{\text{total}}$, which yields

$$\boldsymbol{F}_{\text{total}}=\begin{bmatrix}F_x\\ F_y\\ F_z\end{bmatrix}=\boldsymbol{F}_g+\boldsymbol{F}_p+\boldsymbol{F}_a+\boldsymbol{F}_l. \tag{6}$$

All forces in Equation (6) are defined in the body frame.

The expressions of the gravitational force and pusher motor force are the same as those for a conventional UAV, which are written as

$$\boldsymbol{F}_g=\begin{bmatrix}-mg\sin\theta\\ mg\cos\theta\sin\phi\\ mg\cos\theta\cos\phi\end{bmatrix} \tag{7}$$

and

$$\boldsymbol{F}_p=\begin{bmatrix}F_{px}\\ 0\\ 0\end{bmatrix}=\begin{bmatrix}C_p\cdot\rho\cdot D^4\left(\frac{\omega_p}{60}\right)^2\\ 0\\ 0\end{bmatrix}, \tag{8}$$

where C_p is the pusher propeller thrust coefficient, ρ is the air density, and D is the propeller diameter.

Fixed-wing aerodynamics is the main subject of study during fixed-wing flight because it is the primary principle for generating forces and moments. These forces and moments ensure the stable flight of the quad-plane. The aerodynamic forces consist of the lift F_L, side force F_S, and drag F_D that are transformed from the stability frame to body frame, which results in

$$\boldsymbol{F}_a = \begin{bmatrix} -\sin\alpha & 0 & \cos\alpha \\ 0 & 1 & 0 \\ \cos\alpha & 0 & \sin\alpha \end{bmatrix} \begin{bmatrix} -F_L \\ F_S \\ -F_D \end{bmatrix} = \begin{bmatrix} -\sin\alpha & 0 & \cos\alpha \\ 0 & 1 & 0 \\ \cos\alpha & 0 & \sin\alpha \end{bmatrix} \begin{bmatrix} -\frac{1}{2}\rho V_a^2 S \cdot C_L(\alpha, \delta_\mathrm{e}, V_a, \omega_1, \omega_2, \omega_3, \omega_4) \\ \frac{1}{2}\rho V_a^2 S \cdot C_S(\alpha, \beta, \delta_\mathrm{r}) \\ -\frac{1}{2}\rho V_a^2 S \cdot C_D(\alpha, \delta_\mathrm{e}, \delta_\mathrm{a}, \delta_\mathrm{r}) \end{bmatrix}, \tag{9}$$

where $\delta_\mathrm{a} = \delta_{\mathrm{a_r}} - \delta_{\mathrm{a_l}}$, and $\delta_\mathrm{r} = \frac{1}{2}(\delta_{\mathrm{r_r}} + \delta_{\mathrm{r_l}})$. The airspeed V_a and aerodynamic coefficients are the most influential factors in aerodynamics. Aerodynamic coefficients of this quad-plane were obtained by CFD analyses, wind tunnel experiments, and flight tests as described in Reference 39. Due to the detailed wind tunnel experiments, comprehensive nonlinear relationships in the coefficients were obtained, and the study of interactions between the fixed wing and lift motors was also conducted. For example, when all actuators are turned on, the airflow through lift motors 1 and 3 results in a lift loss of the fixed wing.[39]

In hover flight, the main source of force is the lift motor. For this quad-plane, two components are studied, namely the thrust T and H-force H:

$$\boldsymbol{F}_l = \begin{bmatrix} -\left(H_{x1}(\omega_1, u) + H_{x2}(\omega_2, u) + H_{x3}(\omega_3, u) + H_{x4}(\omega_4, u)\right) \\ -\left(H_{y1}(\omega_1, v) + H_{y2}(\omega_2, v) + H_{y3}(\omega_3, v) + H_{y4}(\omega_4, v)\right) \\ -\left(T_1(\omega_1, u, v, w) + T_2(\omega_2, \omega_3, u, v, w) + T_3(\omega_3, u, v, w) + T_4(\omega_4, \omega_1, u, v, w)\right) \end{bmatrix}. \tag{10}$$

where $T_{1,2,3,4}$ are the thrusts along the negative z-axis in the body frame generated by the four lift motors, whereas $H_{x1,2,3,4}$ and $H_{y1,2,3,4}$ are the drags of the four lift motors along the x-axis and y-axis in the body frame, respectively.[40]

The total moment $\boldsymbol{M}_\mathrm{total}$ is expressed as

$$\boldsymbol{M}_\mathrm{total} = \begin{bmatrix} M_\mathrm{roll} \\ M_\mathrm{pitch} \\ M_\mathrm{yaw} \end{bmatrix} = \boldsymbol{M}_a + \boldsymbol{M}_l, \tag{11}$$

where $\boldsymbol{M}_a$ denotes the aerodynamic moment, and $\boldsymbol{M}_l$ refers to the moment caused by lift motors. Since the moments are all measured in the body frame, there is no frame transformation in the moment expressions.

The aerodynamic moments are given by

$$\boldsymbol{M}_a = \begin{bmatrix} \frac{1}{2}\rho V_a^2 Sb \cdot C_l(\alpha, \beta, \delta_\mathrm{a}, p, r, \omega_1, \omega_2, \omega_3, \omega_4) \\ \frac{1}{2}\rho V_a^2 Sc \cdot C_m(\alpha, \delta_\mathrm{e}, q, u, v, \omega_1, \omega_2, \omega_3, \omega_4) \\ \frac{1}{2}\rho V_a^2 Sb \cdot C_n(\alpha, \beta, \delta_\mathrm{a}, \delta_\mathrm{r}, p, r) \end{bmatrix} \tag{12}$$

with aerodynamic coefficients C_l, C_m, and C_n.

Moments generated by lift motors are expressed as

$$\boldsymbol{M}_l = \begin{bmatrix} d_y \cdot (T_3 + T_2 - T_1 - T_4) - d_z \cdot (H_{y1} + H_{y2} + H_{y3} + H_{y4}) \\ d_x \cdot (T_1 + T_3 - T_2 - T_4) + d_z \cdot (H_{x1} + H_{x2} + H_{x3} + H_{x4}) \\ d_y \cdot (H_{x1} + H_{x4} - H_{x2} - H_{x3}) + d_x \cdot (H_{y2} + H_{y4} - H_{y1} - H_{y3}) + N_{Mt} \end{bmatrix}, \tag{13}$$

where N_{Mt} indicates the yaw moment caused by the rotational speed difference between the individual lift motors.[41]

3 | INCREMENTAL NONLINEAR DYNAMIC INVERSION

Compared with nonlinear dynamic inversion (NDI), incremental nonlinear dynamic inversion (INDI) is derived at the current state and control input.[26] The specific derivation process is as follows.

A general nonlinear system is expressed as Equation (1). Linearization of this nonlinear system can be performed at the current point in time based on a first-order Taylor series expansion. Neglecting higher-order terms, the expression results in

$$\dot{\boldsymbol{x}} \approx \dot{\boldsymbol{x}}_0 + \frac{\partial \boldsymbol{f}(\boldsymbol{x},\boldsymbol{u})}{\partial \boldsymbol{x}}\Big|_{\boldsymbol{x}=\boldsymbol{x}_0,\boldsymbol{u}=\boldsymbol{u}_0}(\boldsymbol{x}-\boldsymbol{x}_0) + \frac{\partial \boldsymbol{f}(\boldsymbol{x},\boldsymbol{u})}{\partial \boldsymbol{u}}\Big|_{\boldsymbol{x}=\boldsymbol{x}_0,\boldsymbol{u}=\boldsymbol{u}_0}(\boldsymbol{u}-\boldsymbol{u}_0), \tag{14}$$

where the variables $\boldsymbol{x}_0$, $\dot{\boldsymbol{x}}_0$, and $\boldsymbol{u}_0$ with subscript '0' represent the values measured at the current point in time, while the variables $\boldsymbol{x}$, $\dot{\boldsymbol{x}}$, and $\boldsymbol{u}$ represent the values calculated for the next point in time.

Using $\boldsymbol{F}(\boldsymbol{x}_0,\boldsymbol{u}_0)$ and $\boldsymbol{G}(\boldsymbol{x}_0,\boldsymbol{u}_0)$ to represent the partial differential part, Equation (14) is expressed as

$$\dot{\boldsymbol{x}} \approx \dot{\boldsymbol{x}}_0 + \boldsymbol{F}(\boldsymbol{x}_0,\boldsymbol{u}_0)(\boldsymbol{x}-\boldsymbol{x}_0) + \boldsymbol{G}(\boldsymbol{x}_0,\boldsymbol{u}_0)(\boldsymbol{u}-\boldsymbol{u}_0). \tag{15}$$

Assuming a small sample time and instantaneous actuators, the time-scale separation principle holds true.[26] According to this principle, the input $\boldsymbol{u}$ changes much faster than the state $\boldsymbol{x}$. Therefore, $\boldsymbol{x} \approx \boldsymbol{x}_0$ and $\boldsymbol{u} \neq \boldsymbol{u}_0$ are assumed. Based on the above assumptions and established relationships, Equation (15) is simplified as

$$\dot{\boldsymbol{x}} = \dot{\boldsymbol{x}}_0 + \boldsymbol{G}(\boldsymbol{x}_0,\boldsymbol{u}_0)(\boldsymbol{u}-\boldsymbol{u}_0). \tag{16}$$

Finally, the control input $\boldsymbol{u}$ is derived by

$$\boldsymbol{u} = \boldsymbol{u}_0 + \boldsymbol{G}^{\dagger}(\boldsymbol{x}_0,\boldsymbol{u}_0)(\boldsymbol{v}-\dot{\boldsymbol{x}}_0), \tag{17}$$

where the virtual control input $\boldsymbol{v}$ is defined by $\boldsymbol{v} = \dot{\boldsymbol{x}}$, and $\boldsymbol{G}^{\dagger}$ denotes the Moore-Penrose pseudoinverse[42] of $\boldsymbol{G}$. Applying this equation, the input to the corresponding real actuator can be solved. The prerequisite for INDI to be applied is that $\dot{\boldsymbol{x}}_0, \boldsymbol{x}_0$, and $\boldsymbol{u}_0$ are measurable.[26] In addition, the pseudoinverse used in this paper is more general and always exists, because it can be applied not only to singular matrices but also to nonsquare matrices.[43] When the matrix is a nonsingular matrix, it is equivalent to the inverse of the matrix. The pseudoinverse is also a control allocation strategy used for actuator-redundant systems.[42]

Through the above derivation process and literature research, INDI-based control methods have the following advantages:

i. Robustness: From the derivation process of INDI, the system matrix $\boldsymbol{F}(\boldsymbol{x}_0,\boldsymbol{u}_0)$ is neglected, indicating that the method is less dependent on the model and can reduce the influence of model uncertainty on the system response.[26]
ii. Wide range of applications: It can also be applied to input nonaffine systems.[30]
iii. Simplicity of design: Gain scheduling is not required because it can adapt to changes in state.[31]
iv. Less computational requirements: It is easy to be deployed and can be applied practically.

4 | CONTROL LAW DESIGN FOR FIXED-WING FLIGHT

In this section, a cascade control structure for fixed-wing flight will be proposed, and control laws will be designed from the inner loop to the outer loop.

4.1 | Control structure

Figure 2 gives a brief overview of the whole control structure for the fixed-wing flight regime. The Path Planner & Manager module sends a desired path command to the Path-Following Algorithm module. With the desired path, the

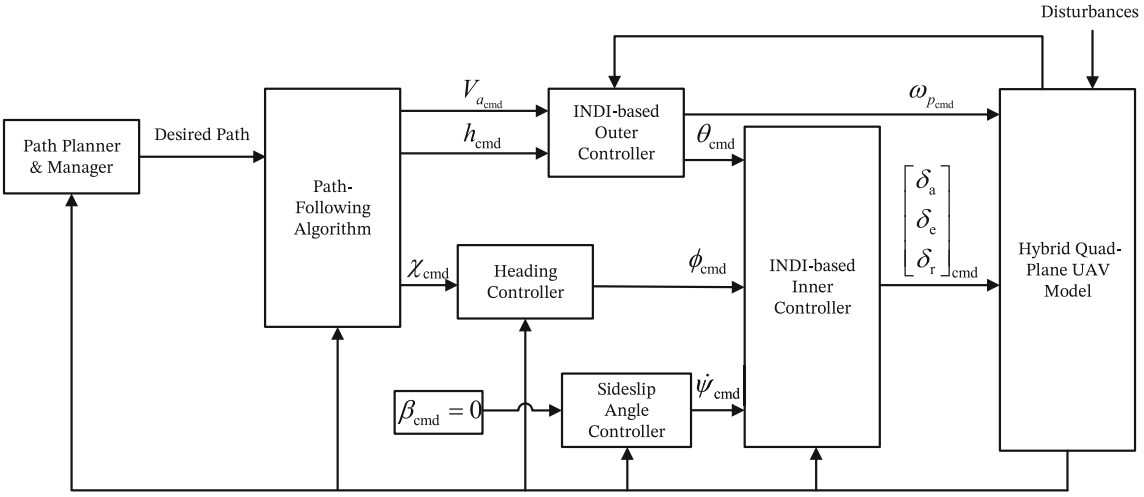

FIGURE 2 Complete control structure of fixed-wing flight

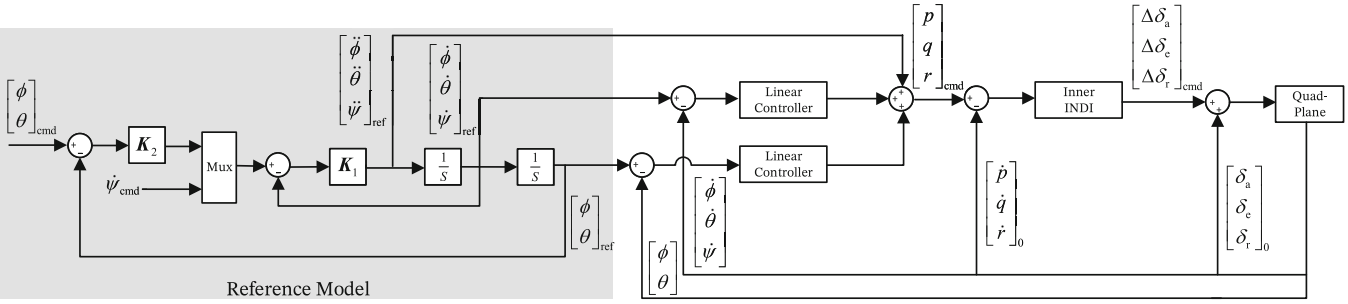

FIGURE 3 INDI-based inner control structure of fixed-wing flight

path-following algorithm commands the airspeed V_a, altitude $h = -p_d$, and course angle χ. Due to the high coupling between the altitude and airspeed, it is impractical to treat them as separate channels during the control law design. Therefore, an INDI-based outer controller is designed to handle it. To ensure coordinated turns during fixed-wing flight, the course angle χ is controlled by the roll angle ϕ, and the sideslip angle β is always maintained to be zero. The deflections of control surfaces can be obtained through the inner INDI-based attitude controller to track desired Euler angle commands. Detailed elaboration of this control structure is given in the following subsections.

4.2 | INDI-based inner controller

The INDI-based inner controller structure is shown in Figure 3. Angular accelerations in the body frame can be obtained from Euler angles through reference models and linear controllers. Then, the deflection commands of the control surfaces are obtained directly from angular accelerations by the INDI module.

4.2.1 | INDI for angular acceleration control

Firstly, the INDI module will be elaborated. Based on Equations (5) and (11), the rotational dynamics for fixed-wing flight is expressed as

$$\boldsymbol{I}\dot{\boldsymbol{\Omega}} + \boldsymbol{\Omega} \times \boldsymbol{I}\boldsymbol{\Omega} = \boldsymbol{M}_a, \tag{18}$$

where $\boldsymbol{\Omega} = [p,\ q,\ r]^\top$. Referring to Subsection 2.2 and ignoring items related to lift motors, the aerodynamic moments can be summarized as

$$\boldsymbol{M}_a = \boldsymbol{M}_{a1}(V_a, \alpha, \beta, p, q, r) + \boldsymbol{M}_{a2}(V_a, \alpha, \beta) \cdot [\delta_\mathrm{a}, \delta_\mathrm{e}, \delta_\mathrm{r}]^\top. \tag{19}$$

Combining Equation (18) with Equation (19),

$$\begin{aligned}\dot{\boldsymbol{\Omega}} &= \boldsymbol{I}^{-1}\left(\boldsymbol{M}_a - \boldsymbol{\Omega} \times \boldsymbol{I}\boldsymbol{\Omega}\right)\\ &= \boldsymbol{I}^{-1}\left(\boldsymbol{M}_{a1}(V_a, \alpha, \beta, p, q, r) - \boldsymbol{\Omega} \times \boldsymbol{I}\boldsymbol{\Omega}\right) + \boldsymbol{I}^{-1}\boldsymbol{M}_{a2}(V_a, \alpha, \beta) \cdot [\delta_\mathrm{a}, \delta_\mathrm{e}, \delta_\mathrm{r}]^\top\\ &= \boldsymbol{F}_f(V_a, \alpha, \beta, \boldsymbol{\Omega}) + \boldsymbol{G}_f(V_a, \alpha, \beta) \cdot [\delta_\mathrm{a}, \delta_\mathrm{e}, \delta_\mathrm{r}]^\top,\end{aligned} \tag{20}$$

where $\boldsymbol{F}_f(V_a, \alpha, \beta, \boldsymbol{\Omega}) = \boldsymbol{I}^{-1}(\boldsymbol{M}_{a1}(V_a, \alpha, \beta, p, q, r) - \boldsymbol{\Omega} \times \boldsymbol{I}\boldsymbol{\Omega})$, and $\boldsymbol{G}_f(V_a, \alpha, \beta) = \boldsymbol{I}^{-1}\boldsymbol{M}_{a2}(V_a, \alpha, \beta)$. For the ease of representation, $[\delta_\mathrm{a}, \delta_\mathrm{e}, \delta_\mathrm{r}]^\top$ is denoted as $\boldsymbol{u}_f$. Then, a Taylor expansion is performed on Equation (20) neglecting the higher-order terms. According to the time-scale separation principle, the terms of the Taylor expansion equation with respect to V_a, α, β, and $\boldsymbol{\Omega}$ can be neglected. So the expansion is simplified as

$$\dot{\boldsymbol{\Omega}} = \dot{\boldsymbol{\Omega}}_0 + \boldsymbol{G}_f(V_{a0}, \alpha_0, \beta_0)(\boldsymbol{u}_f - \boldsymbol{u}_{f0}), \tag{21}$$

where the zero-order term is expressed as $\dot{\boldsymbol{\Omega}}_0 = \boldsymbol{F}_f(V_{a0}, \alpha_0, \beta_0, \boldsymbol{\Omega}_0) + \boldsymbol{G}_f(V_{a0}, \alpha_0, \beta_0) \cdot \boldsymbol{u}_{f0}$.

Setting $\dot{\boldsymbol{\Omega}}$ as the virtual input $\boldsymbol{v}_f$, $\boldsymbol{u}_f$ is derived by

$$\boldsymbol{u}_f = \boldsymbol{u}_{f0} + \boldsymbol{G}_f^\dagger(V_{a0}, \alpha_0, \beta_0)(\boldsymbol{v}_f - \dot{\boldsymbol{\Omega}}_0), \tag{22}$$

where $\boldsymbol{G}_f(V_{a0}, \alpha_0, \beta_0)$ is a 3×3 nonsingular matrix because the airspeed and control surface coefficients are not zero in fixed-wing flight.

According to Equation (22), INDI for the attitude control is achieved. Desired control inputs are derived by the virtual control inputs, namely angular accelerations ($\dot{p},\ \dot{q},\ \dot{r}$). As shown in Figure 3, the reference model and linear controller modules are utilized to generate the desired virtual control inputs.

4.2.2 | Reference model and linear controller

Reference models are commonly used to create demanded reference trajectories for command inputs in a dynamic inversion based controller design process.[44] In the attitude control law design, they are in a linear second-order form:

$$G_{\mathrm{ref}}(s) = \frac{K_1 K_2}{s^2 + K_1 s + K_1 K_2} = \frac{\omega_n^2}{s^2 + 2\zeta\omega_n s + \omega_n^2}. \tag{23}$$

Parameters in Equation (23) should be defined such that the reference models satisfy the quad-plane Flying and Handling Quality requirements.[31] Because the flight data analysis of this quad-plane is not sufficient at this research stage, an integrated reference model[44] is hard to be established. Therefore, referring to Reference 31, the parameter values are the best results selected in the simulation process. The values chosen for the roll, pitch, and yaw channels are listed in Table 2. Depending on the flight requirements, the system responds faster in roll and pitch motion than in yaw motion. Since the yaw angle rate is selected as the input in the yaw channel (see Figure 3), only K_1 is needed to be given.

TABLE 2 Reference model parameters of fixed-wing flight

Axis	ζ	ω_n	K_1	K_2
Roll & Pitch	0.9	2	3.6	1.11
Yaw	0.9	0.8	1.44	

TABLE 3 Linear controller gains of fixed-wing flight in the inner loop

Gain	Value	Gain	Value	Gain	Value
K_{ϕ_P}	8	K_{θ_P}	8	K_{ψ_P}	2.5
K_{ϕ_I}	1	K_{θ_I}	1		
$K_{\dot{\phi}_P}$	7	$K_{\dot{\theta}_P}$	7		

The role of linear controllers is to eliminate tracking errors. Linear controllers utilized in this article are based on the PID control law. The Euler angle acceleration values are fed forward to virtual controls to minimize the adjusting time of controllers. Control laws for roll, pitch, and yaw channels are as follows:

$$\begin{aligned}
\dot{p}_{\text{cmd}} &= \left(K_{\phi_P} + \frac{K_{\phi_I}}{s}\right)(\phi_{\text{ref}} - \phi) + K_{\dot{\phi}_P}(\dot{\phi}_{\text{ref}} - \dot{\phi}) + \ddot{\phi}_{\text{ref}} \\
\dot{q}_{\text{cmd}} &= \left(K_{\theta_P} + \frac{K_{\theta_I}}{s}\right)(\theta_{\text{ref}} - \theta) + K_{\dot{\theta}_P}(\dot{\theta}_{\text{ref}} - \dot{\theta}) + \ddot{\theta}_{\text{ref}} \\
\dot{r}_{\text{cmd}} &= K_{\dot{\psi}_P}(\dot{\psi}_{\text{ref}} - \dot{\psi}) + \ddot{\psi}_{\text{ref}}.
\end{aligned} \tag{24}$$

The relevant parameter values are shown in Table 3. The proportional gain is tuned according to the system response speed, the integral gain can be tuned to avoid steady-state errors, and the derivative gain can be tuned to reduce oscillations in the system response.[45] In addition, these three gains need to be coordinated to obtain the desired effect.

4.3 | Outer controller

The outer controller consists of an INDI-based outer controller, a heading controller, and a sideslip angle controller (see Figure 2). Firstly, the INDI-based outer controller for the airspeed and altitude control will be elaborated in this section. As the airspeed and altitude are mainly controlled by the pusher motor and elevator, the lateral motion is neglected ($\beta = 0, \phi = 0$) during deriving INDI. According to the dynamic equations in Section 2 and assuming no wind ($V_g = V_a$), the force balance equations are

$$\begin{cases}
\dot{V}_a = \frac{F_{px} - F_D}{m} - g\sin\gamma \\
\dot{\gamma} = \frac{F_L}{mV_a} - \frac{g}{V_a}\cos\gamma
\end{cases}, \tag{25}$$

with F_{px} defined in Equation (8), F_L and F_D defined in Equation (9), and the flight path angle γ. The direct effect of control surface deflection on aerodynamic forces is small, but it dramatically affects aerodynamic moments. For example, when the elevator deflection changes, a variation in the pitch moment occurs, which changes the magnitude of the angle of attack, resulting in a difference in the lift force. Therefore, control surface deflections are chosen as outputs of the inner loop, and all the terms in the above equations related to the deflections are neglected. In this case, Equation (25) is derived as

$$\begin{cases}
\dot{V}_a = \frac{F_{px}}{m} - \frac{1}{2m}\rho V_a^2 S\left(C_{D\alpha 2}\cdot\alpha^2 + C_{D\alpha 1}\cdot\alpha + C_{D\alpha 0}\right) - g\sin\gamma \\
\dot{\gamma} = \frac{1}{2m}\rho V_a S\left(C_{L\alpha 1}\cdot\alpha + C_{L\alpha 0}\right) - \frac{g}{V_a}\cos\gamma
\end{cases}. \tag{26}$$

Since the longitudinal angle input to the inner attitude controller is based on the pitch angle, the angle of attack α is converted into the pitch angle θ with $\alpha = \theta - \gamma$. The Taylor expansion of Equation (26) at the current point of time, preserving the first-order terms and assuming the time-scale separation principle holds, is shown as

$$\begin{bmatrix} \dot{V}_a - \dot{V}_{a0} \\ \dot{\gamma} - \dot{\gamma}_0 \end{bmatrix} = \begin{bmatrix} -\frac{1}{2m}\rho S\left(2C_{D\alpha 2}\cdot(\theta_0 - \gamma_0) + C_{D\alpha 1}\right)\cdot V_{a0}^2 & \frac{1}{m} \\ \frac{1}{2m}\rho S C_{L\alpha 1}\cdot V_{a0} & 0 \end{bmatrix} \begin{bmatrix} \theta - \theta_0 \\ F_{px} - F_{Px0} \end{bmatrix}. \tag{27}$$

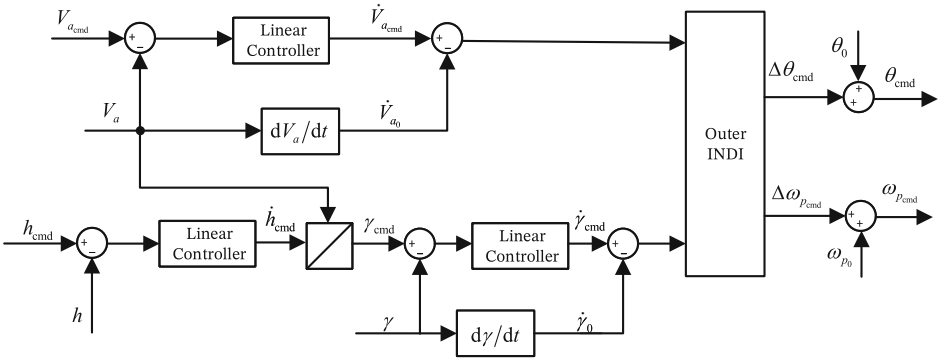

FIGURE 4 INDI-based outer control structure of fixed-wing flight

TABLE 4 Controller gains of fixed-wing flight in the outer loop

Gain	Value	Gain	Value	Gain	Value	Gain	Value	Gain	Value
$K_{V_{a_P}}$	2	K_{h_P}	1	K_{γ_P}	0.5	K_{χ_P}	5	K_{β_P}	−10
$K_{V_{a_I}}$	0.1			K_{γ_I}	0.05	K_{χ_I}	1	K_{β_I}	−3
$K_{V_{a_D}}$	5			K_{γ_D}	0.1	K_{χ_D}	5	K_{β_D}	−5

Setting $\boldsymbol{x}_i = [V_a,\ \gamma]^\top$ and $\boldsymbol{u}_i = [\theta,\ F_{px}]^\top$, Equation (27) is simplified as

$$\dot{\boldsymbol{x}}_i - \dot{\boldsymbol{x}}_{i0} = \boldsymbol{B}_i(\boldsymbol{u}_i - \boldsymbol{u}_{i0}). \tag{28}$$

Therefore,

$$\boldsymbol{u}_i = \boldsymbol{u}_{i0} + \boldsymbol{B}_i^{\dagger}(\boldsymbol{v}_i - \dot{\boldsymbol{x}}_{i0}), \tag{29}$$

where $\boldsymbol{v}_i = [\dot{V}_a,\ \dot{\gamma}]^\top$ is the virtual input, and $\boldsymbol{B}_i$ is a 2×2 nonsingular matrix because the airspeed and aerodynamic coefficients always exist in fixed-wing flight. The detailed control structure is presented in Figure 4. As the flight path angle γ of the quad-plane is small, the command value of flight path angle γ_{cmd} can be derived by $\dot{h} = V_a \sin\gamma = V_a\gamma$. The output, pusher motor speed, is calculated from F_{px} using Equation (8).

The linear controllers in Figure 4 and the heading and sideslip angle controllers in the outer loop are designed based on the conventional PID controllers and expressed in Equation (30). The corresponding controller gains are listed in Table 4.

$$\begin{aligned}
\dot{V}_{a_{\text{cmd}}} &= \left(K_{V_{a_P}} + \frac{K_{V_{a_I}}}{s} + K_{V_{a_D}}s\right)(V_{a_{\text{cmd}}} - V_a),\\
\dot{h}_{\text{cmd}} &= K_{h_P}(h_{\text{cmd}} - h),\\
\dot{\gamma}_{\text{cmd}} &= \left(K_{\gamma_P} + \frac{K_{\gamma_I}}{s} + K_{\gamma_D}s\right)(\gamma_{\text{cmd}} - \gamma),\\
\phi_{\text{cmd}} &= \left(K_{\chi_P} + \frac{K_{\chi_I}}{s} + K_{\chi_D}s\right)(\chi_{\text{cmd}} - \chi),\\
\dot{\psi}_{\text{cmd}} &= \left(K_{\beta_P} + \frac{K_{\beta_I}}{s} + K_{\beta_D}s\right)(\beta_{\text{cmd}} - \beta).
\end{aligned} \tag{30}$$

5 | CONTROL LAW DESIGN FOR HOVER FLIGHT

In this section, the control law design for hover flight will be introduced. Firstly, a whole cascade control structure will be proposed. Subsequently, the detailed control law design will be evolved from the inner loop to the outer loop.

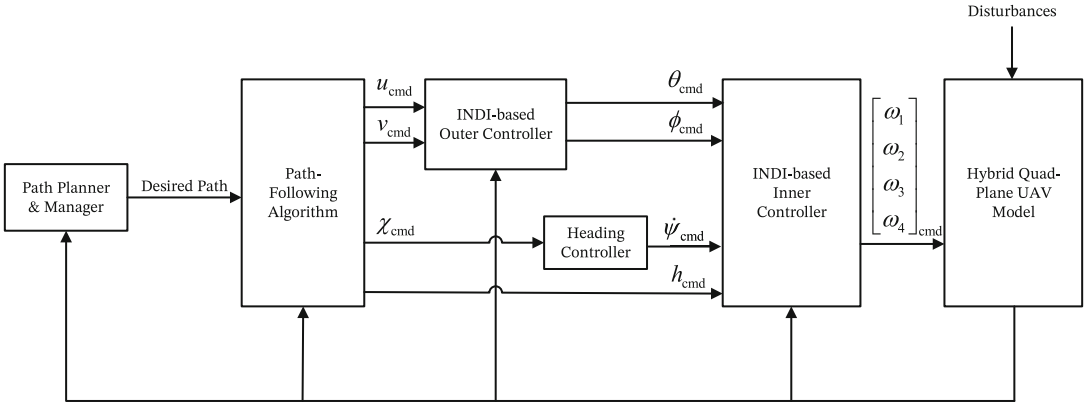

FIGURE 5 Complete control structure of hover flight

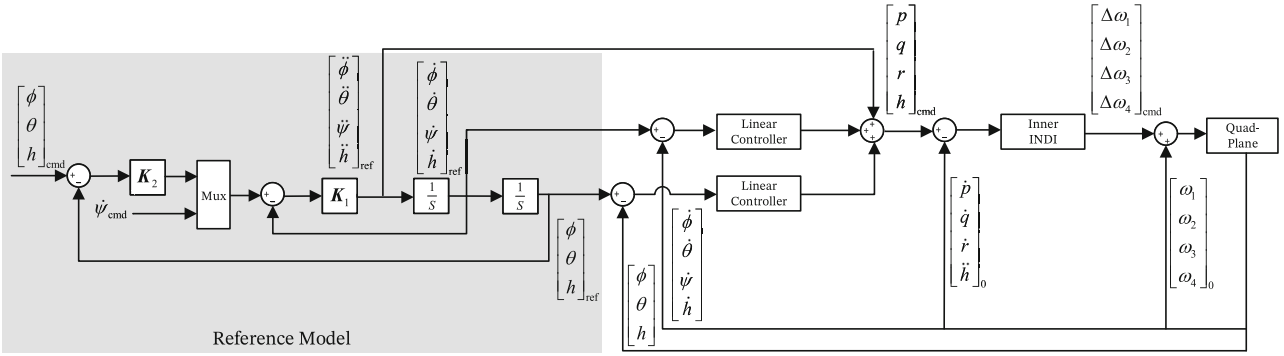

FIGURE 6 INDI-based inner control structure of hover flight

5.1 | Control structure

The complete control structure of the hover flight regime from the inner loop to the outer loop is shown in Figure 5. Similar to the fixed-wing flight regime, the Path-Following Algorithm block outputs the corresponding commands, namely velocities u and v, course angle χ, and altitude h. The control structure is cascaded. In the outer loop, an INDI-based controller generates corresponding roll angle ϕ and pitch angle θ to the inner loop according to u and v commands, and the heading controller gives out the reference yaw angle rate $\dot{\psi}$. Combined with the altitude h, the INDI-based inner controller computes the lift motor rotational speeds $(\omega_1, \omega_2, \omega_3, \omega_4)$.

5.2 | INDI-based inner controller

The control structure of the INDI-based inner controller is shown in Figure 6. Like the inner loop for fixed-wing flight, the inner loop for hover flight relies on a reference model to generate the inputs required by the linear controller. Then, the rotational speeds of the four lift motors can be obtained from the INDI module. The INDI for angular and vertical acceleration control will be derived separately because they are based on moment and force balance, respectively.

5.2.1 | INDI for angular acceleration control

The moment balance of the quad-plane in hover flight is given by

$$\boldsymbol{I}\dot{\boldsymbol{\Omega}} + \boldsymbol{\Omega} \times \boldsymbol{I}\boldsymbol{\Omega} = \boldsymbol{M}_l, \tag{31}$$

where $\boldsymbol{M}_l$, defined in Equation (13), includes the moments produced by lift motors along three axes in the body frame. The aerodynamic moment is neglected due to its small effect during hover flight.

Rotational speeds ($\omega_1,\ \omega_2,\ \omega_3,\ \omega_4$) are the control inputs in hover flight. In the detailed expression of $\boldsymbol{M}_l$, the rotational speeds can be divided into three forms, namely $\boldsymbol{\omega} = [\omega_1,\ \omega_2,\ \omega_3,\ \omega_4]^\top$, $\boldsymbol{\omega}^2 = [\omega_1^2,\ \omega_2^2,\ \omega_3^2,\ \omega_4^2]^\top$, and $\tilde{\boldsymbol{\omega}} = [\omega_4\omega_1,\ \omega_3\omega_2,\ \omega_2\omega_3,\ \omega_1\omega_4]^\top$. Thus, extracting these rotational speeds yields

$$\boldsymbol{M}_l = \boldsymbol{M}_{la}\boldsymbol{\omega}^2 + \boldsymbol{M}_{lb}\boldsymbol{\omega} + \boldsymbol{M}_{lc}\tilde{\boldsymbol{\omega}}, \tag{32}$$

where $\boldsymbol{M}_{la}$, $\boldsymbol{M}_{lb}$, and $\boldsymbol{M}_{lc}$ are the coefficient matrices associated with $\boldsymbol{\omega}^2$, $\boldsymbol{\omega}$, and $\tilde{\boldsymbol{\omega}}$ in the $\boldsymbol{M}_l$ expression, respectively. Then, Equation (31) is derived as

$$\dot{\boldsymbol{\Omega}} = \boldsymbol{I}^{-1}\boldsymbol{M}_{la}\boldsymbol{\omega}^2 + \boldsymbol{I}^{-1}\boldsymbol{M}_{lb}\boldsymbol{\omega} + \boldsymbol{I}^{-1}\boldsymbol{M}_{lc}\tilde{\boldsymbol{\omega}} - \boldsymbol{I}^{-1}(\boldsymbol{\Omega}\times\boldsymbol{I}\boldsymbol{\Omega}) = \boldsymbol{G}_a\boldsymbol{\omega}^2 + \boldsymbol{G}_b\boldsymbol{\omega} + \boldsymbol{G}_c\tilde{\boldsymbol{\omega}} - \boldsymbol{I}^{-1}(\boldsymbol{\Omega}\times\boldsymbol{I}\boldsymbol{\Omega}). \tag{33}$$

Taylor expansion of Equation (33) and ignoring the higher order terms and all partial derivative terms that are independent of the actuator speed $\boldsymbol{\omega}$ yield

$$\dot{\boldsymbol{\Omega}} = \dot{\boldsymbol{\Omega}}_0 + \left(2\boldsymbol{G}_a\mathrm{diag}(\boldsymbol{\omega}_0) + \boldsymbol{G}_b + \boldsymbol{G}_c\hat{\boldsymbol{\omega}}_0\right)(\boldsymbol{\omega} - \boldsymbol{\omega}_0), \tag{34}$$

where $\dot{\boldsymbol{\Omega}}_0 = \boldsymbol{G}_a\boldsymbol{\omega}_0^2 + \boldsymbol{G}_b\boldsymbol{\omega}_0 + \boldsymbol{G}_c\tilde{\boldsymbol{\omega}}_0 - \boldsymbol{I}^{-1}(\boldsymbol{\Omega}_0\times\boldsymbol{I}\boldsymbol{\Omega}_0)$ and

$$\hat{\boldsymbol{\omega}} = \begin{bmatrix} \omega_4 & 0 & 0 & \omega_1 \\ 0 & \omega_3 & \omega_2 & 0 \\ 0 & \omega_3 & \omega_2 & 0 \\ \omega_4 & 0 & 0 & \omega_1 \end{bmatrix}. \tag{35}$$

Transforming $\boldsymbol{u}_h = \boldsymbol{\omega}$, $\boldsymbol{v}_{h1} = \dot{\boldsymbol{\Omega}}$ as virtual input, and $\boldsymbol{G}_h = 2\boldsymbol{G}_a\mathrm{diag}(\boldsymbol{\omega}_0) + \boldsymbol{G}_b + \boldsymbol{G}_c\hat{\boldsymbol{\omega}}_0$, Equation (34) results in

$$\boldsymbol{u}_h = \boldsymbol{u}_{h0} + \boldsymbol{G}_h^{\dagger}(\boldsymbol{v}_{h1} - \dot{\boldsymbol{\Omega}}_0). \tag{36}$$

With the desired angular acceleration $\boldsymbol{v}_{h1}$, the corresponding desired rotational speeds of the four lift motors can be calculated with Equation (36).

5.2.2 | INDI for vertical acceleration control

The force balance of the quad-plane along z axis in the inertial frame is

$$F_z = m(g + \dot{V}_z) = (T_1 + T_2 + T_3 + T_4)\cos\phi\cos\theta + (H_{x1} + H_{x2} + H_{x3} + H_{x4})\sin\theta - (H_{y1} + H_{y2} + H_{y3} + H_{y4})\sin\phi\cos\theta, \tag{37}$$

where the positive direction of acceleration $\dot{V}_z$ is upward. Since the thrust and H-force expressions depend on $\boldsymbol{\omega}^2$, $\boldsymbol{\omega}$, and $\tilde{\boldsymbol{\omega}}$, Equation (37) can be rewritten as

$$F_z = \boldsymbol{F}_{za}\boldsymbol{\omega}^2 + \boldsymbol{F}_{zb}\boldsymbol{\omega} + \boldsymbol{F}_{zc}\tilde{\boldsymbol{\omega}}, \tag{38}$$

where $\boldsymbol{F}_{za}$, $\boldsymbol{F}_{zb}$, and $\boldsymbol{F}_{zc}$ represent the coefficient matrices associated with $\boldsymbol{\omega}^2$, $\boldsymbol{\omega}$, and $\tilde{\boldsymbol{\omega}}$ in the F_z expression. Combined with Equation (37), the expression for $\dot{V}_z$ is given by

$$\dot{V}_z = \frac{1}{m}(\boldsymbol{F}_{za}\boldsymbol{\omega}^2 + \boldsymbol{F}_{zb}\boldsymbol{\omega} + \boldsymbol{F}_{zc}\tilde{\boldsymbol{\omega}}) - g. \tag{39}$$

With Taylor expansion of Equation (39), ignoring the higher order terms and terms independent of lift motor rotational speeds,

$$\dot{V}_z - \dot{V}_{z0} = \frac{1}{m}\left(2\boldsymbol{F}_{za}\mathrm{diag}(\boldsymbol{\omega}_0) + \boldsymbol{F}_{zb} + \boldsymbol{F}_{zc}\hat{\boldsymbol{\omega}}_0\right)(\boldsymbol{\omega} - \boldsymbol{\omega}_0), \tag{40}$$

TABLE 5 Reference model parameters of hover flight

Axis	ζ	ω_n	K_1	K_2
Roll & Pitch	0.8	2.4	3.84	1.5
Yaw	0.8	1	1.6	
Altitude	0.8	1	1.6	0.625

where $\dot{V}_{z0} = \frac{1}{m}(\boldsymbol{F}_{za}\boldsymbol{\omega}_0^2 + \boldsymbol{F}_{zb}\boldsymbol{\omega}_0 + \boldsymbol{F}_{zc}\tilde{\boldsymbol{\omega}}_0) - g$ is derived. Substituting v_{h2} for $\dot{V}_z$ as a virtual input and $\boldsymbol{u}_h$ for $\boldsymbol{\omega}$ as the output of the INDI, and setting $\boldsymbol{F}_h = \frac{1}{m}\left(2\boldsymbol{F}_{za}\mathrm{diag}(\boldsymbol{\omega}_0) + \boldsymbol{F}_{zb} + \boldsymbol{F}_{zc}\hat{\boldsymbol{\omega}}_0\right)$ yield

$$\boldsymbol{u}_h = \boldsymbol{u}_{h0} + \boldsymbol{F}_h^{\dagger}(v_{h2} - \dot{V}_{z0}). \tag{41}$$

With the desired vertical acceleration v_{h2}, the corresponding desired rotational speeds of the four lift motors can be calculated.

For the angular and vertical acceleration control, the rotational speeds of lift motors satisfy the linear superposition relationship. The rotational speeds of lift motors calculated by INDI based on the desired angular and vertical acceleration can be directly superimposed. Thus, combining Equations (36) and (41), the inner INDI is derived as

$$\boldsymbol{u}_h = \boldsymbol{u}_{h0} + \begin{bmatrix}\boldsymbol{G}_h \\ \boldsymbol{F}_h\end{bmatrix}^{\dagger}\begin{bmatrix}\boldsymbol{v}_{h1} - \dot{\boldsymbol{\Omega}}_0 \\ v_{h2} - \dot{V}_{z0}\end{bmatrix}, \tag{42}$$

where $[\boldsymbol{G}_h,\ \boldsymbol{F}_h]^{\top}$ is a 4×4 nonsingular matrix because the coefficients with respect to lift motors are not zero.

5.2.3 | Reference model and linear controller

As shown in Figure 6, reference models combined with linear controllers give the virtual control signals ($\dot{p},\ \dot{q},\ \dot{r},\ \ddot{h}$) to the inner INDI. The reference model expression is shown in Equation (23), and the values selected for the roll, pitch, yaw, and altitude channels are listed in Table 5. In the yaw channel, the yaw angle rate is selected as the input (see Figure 6), so only K_1 is used. Depending on flight requirements, pitch and roll responses are faster than yaw and altitude responses. Also, the quad-plane in hover flight is slightly more responsive than in fixed-wing flight.

Similar to the fixed-wing flight regime, linear control laws are designed based on PID control laws with feedforward, and the expressions are

$$\begin{aligned}
\dot{p}_{\mathrm{cmd}} &= \left(K_{\phi_P} + \frac{K_{\phi_I}}{s}\right)(\phi_{\mathrm{ref}} - \phi) + \left(K_{\dot{\phi}_P} + K_{\dot{\phi}_D}s\right)(\dot{\phi}_{\mathrm{ref}} - \dot{\phi}) + \ddot{\phi}_{\mathrm{ref}}, \\
\dot{q}_{\mathrm{cmd}} &= \left(K_{\theta_P} + \frac{K_{\theta_I}}{s}\right)(\theta_{\mathrm{ref}} - \theta) + \left(K_{\dot{\theta}_P} + K_{\dot{\theta}_D}s\right)(\dot{\theta}_{\mathrm{ref}} - \dot{\theta}) + \ddot{\theta}_{\mathrm{ref}}, \\
\dot{r}_{\mathrm{cmd}} &= \left(K_{\dot{\psi}_P} + K_{\dot{\psi}_D}s\right)(\dot{\psi}_{\mathrm{ref}} - \dot{\psi}) + \ddot{\psi}_{\mathrm{ref}}, \\
\ddot{h}_{\mathrm{cmd}} &= K_{h_P}(h_{\mathrm{ref}} - h) + \left(K_{\dot{h}_P} + K_{\dot{h}_D}s\right)(\dot{h}_{\mathrm{ref}} - \dot{h}) + \ddot{h}_{\mathrm{ref}}.
\end{aligned} \tag{43}$$

Corresponding gains are shown in Table 6.

5.3 | Outer controller

As shown in Figure 5, the outer controller includes an INDI-based outer controller and a heading controller. Firstly, the INDI-based outer controller will be elaborated. The control structure is shown in Figure 7. It can be seen that the desired pitch angle θ and roll angle ϕ are the outputs of this module.

TABLE 6 Linear controller gains of hover flight in the inner loop

Gain	Value	Gain	Value	Gain	Value	Gain	Value
K_{ϕ_P}	10	K_{θ_P}	15	K_{ψ_P}	2.5	K_{h_P}	50
K_{ϕ_I}	0.5	K_{θ_I}	1	K_{ψ_D}	2.5	$K_{\dot{h}_P}$	10
$K_{\dot{\phi}_P}$	10	$K_{\dot{\theta}_P}$	15			$K_{\dot{h}_D}$	5
$K_{\dot{\phi}_D}$	5	$K_{\dot{\theta}_D}$	5				

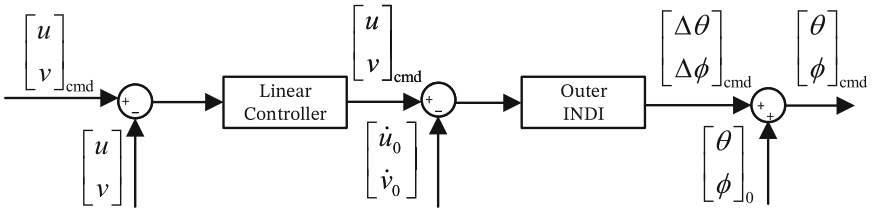

FIGURE 7 INDI-based outer control structure of hover flight

According to Equation (4) and neglecting the cross product part which has no influence on the outer INDI derivation of hover flight, the force balance for the quad-plane along x- and y-axes in the body frame is simplified as

$$m\begin{bmatrix}\dot{u}\\ \dot{v}\end{bmatrix}=\begin{bmatrix}\cos\theta\cos\psi & \cos\theta\sin\psi & -\sin\theta\\ \sin\phi\sin\theta\cos\psi-\cos\phi\sin\psi & \sin\phi\sin\theta\sin\psi+\cos\phi\cos\psi & \sin\phi\cos\theta\end{bmatrix}\begin{bmatrix}0\\0\\mg\end{bmatrix}, \tag{44}$$

where the force is obtained by transforming gravity from the inertial frame into the body frame. Equation (44) can be derived as

$$\begin{cases}\dot{u}=-g\cdot\sin\theta\\ \dot{v}=g\cdot\sin\phi\cos\theta\end{cases}. \tag{45}$$

Assuming that the principle of time-scale separation is satisfied, Equation (45) according to INDI is given by

$$\begin{bmatrix}\dot{u}-\dot{u}_0\\ \dot{v}-\dot{v}_0\end{bmatrix}=\begin{bmatrix}0 & -g\cdot\cos\theta_0\\ g\cdot\cos\phi_0\cos\theta_0 & -g\cdot\sin\phi_0\sin\theta_0\end{bmatrix}\begin{bmatrix}\phi-\phi_0\\ \theta-\theta_0\end{bmatrix}. \tag{46}$$

Setting $\boldsymbol{x}_j=[u,\ v]^\top$, $\boldsymbol{v}_j=\dot{\boldsymbol{x}}_j$, and $\boldsymbol{u}_j=[\phi,\ \theta]^\top$, Equation (46) can be converted into INDI form:

$$\boldsymbol{u}_j=\boldsymbol{u}_{j0}+\boldsymbol{B}_j^{\dagger}(\boldsymbol{v}_j-\dot{\boldsymbol{x}}_{j0}), \tag{47}$$

where $\boldsymbol{B}_j$ is a 2×2 nonsingular matrix because the pitch and roll angles vary between $-30°$ and $30°$ during the quad-plane mission.

The linear controller in Figure 7 and the heading controller in the outer loop are based on PID controllers:

$$\begin{aligned}\dot{u}_{\text{cmd}}&=\left(K_{u_P}+K_{u_D}s\right)(u_{\text{cmd}}-u),\\ \dot{v}_{\text{cmd}}&=\left(K_{v_P}+\frac{K_{v_I}}{s}+K_{v_D}s\right)(v_{\text{cmd}}-v),\\ \dot{\psi}_{\text{cmd}}&=\left(K_{\chi_P}+\frac{K_{\chi_I}}{s}+K_{\chi_D}s\right)(\chi_{\text{cmd}}-\chi),\end{aligned} \tag{48}$$

where the controller gains are presented in Table 7.

TABLE 7 Controller gains of hover flight in the outer loop

Gain	Value	Gain	Value	Gain	Value
K_{u_P}	1.5	K_{v_P}	1	K_{χ_P}	0.5
K_{u_D}	1	K_{v_I}	0.01	K_{χ_I}	0.05
		K_{v_D}	0.7	K_{χ_D}	0.5

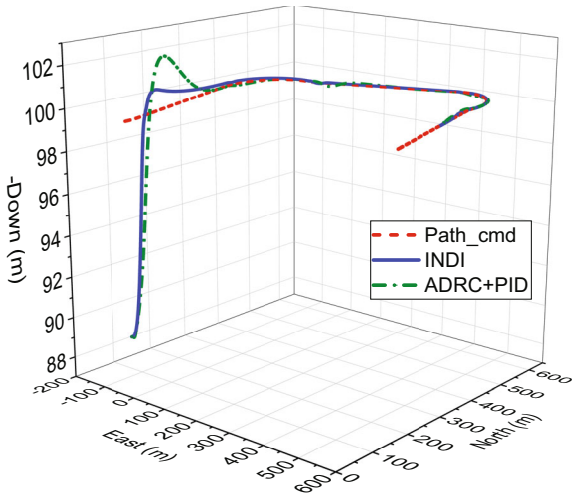

FIGURE 8 Path-following performance of fixed-wing flight in the nominal case

6 | SIMULATION RESULTS

In this section, simulations are conducted to evaluate the autonomous path-following performance of the proposed control laws for the fixed-wing and hover flight regimes. The desired paths are generated by the Path Planner & Manager module. The path planner generates a sequence of waypoints to achieve some purposes, for example, avoiding obstacles, while the objective of the path manager is to convert waypoints into straight-line paths and circular arcs for UAVs to follow.[38] The path-following algorithm used in this simulation is the vector field algorithm.[46] Wind gust disturbances and model uncertainties are also considered in the simulation to verify the robustness of the control law. The control law designed based on ADRC and PID control methods is considered as a comparison group. The sampling frequency of the simulation is 100 Hz.

6.1 | Path following in fixed-wing flight

Three sets of simulation experiments are carried out to verify the performance and robustness of the fixed-wing flight control law: nominal case, wind gust disturbance case, and model parameter uncertainty case. Moreover, simulations of the control law designed based on ADRC and PID control methods are also conducted. For the fixed-wing flight control structure (see Figure 2), the control laws for pitch angle θ, roll angle ϕ, and sideslip angle β are designed by the ADRC method, whereas the control laws for airspeed V_a, altitude h, and course angle χ are designed based on PID controllers.

6.1.1 | Nominal case

In fixed-wing flight, the path-following objective is to follow the command path given in Figure 8. It contains straight-line and circular paths, which are the most commonly used in path-following tasks. Additionally, the airspeed is required to remain constant most of the time during path following to accomplish tasks such as irrigation effectively. Thus, the

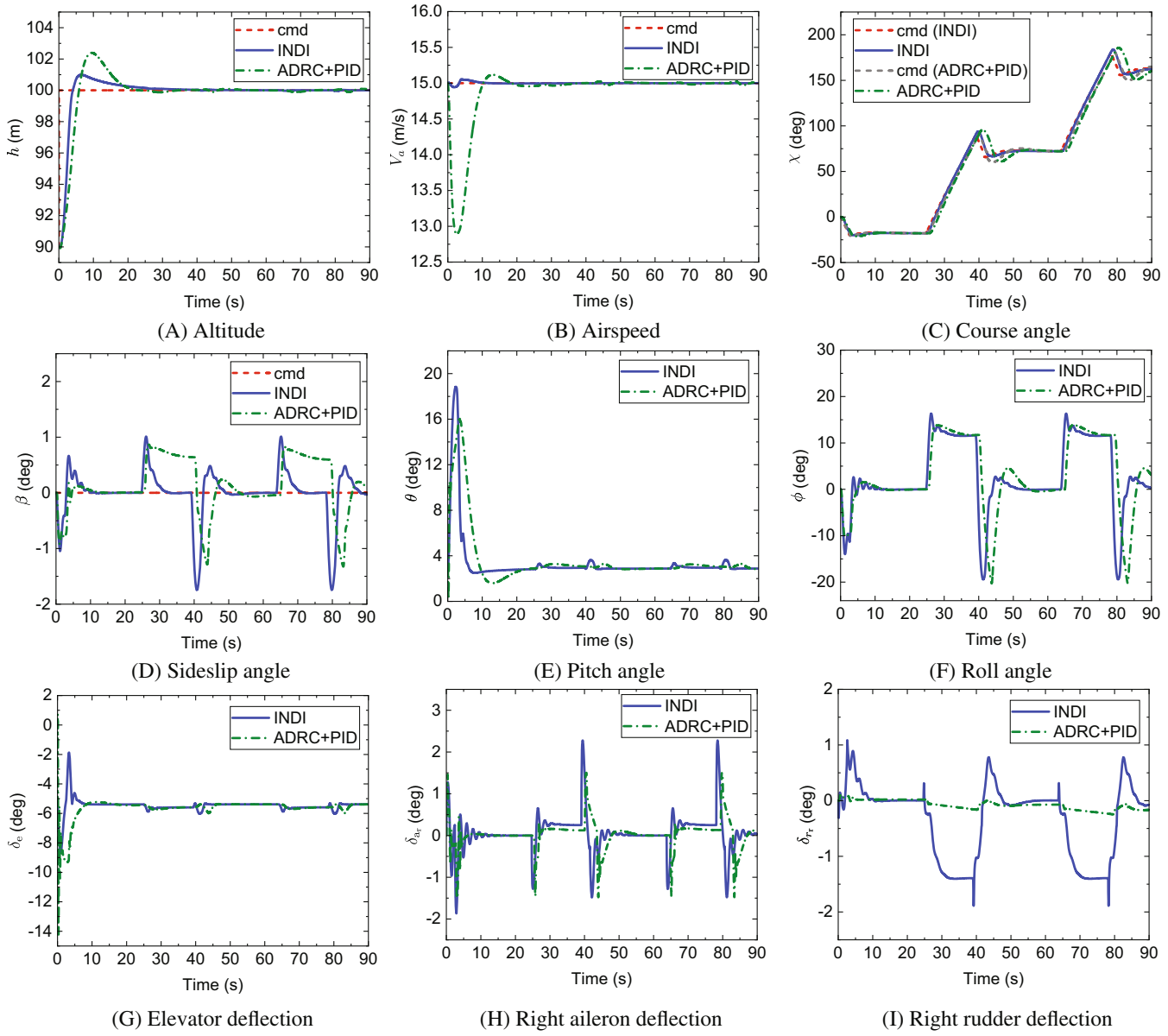

FIGURE 9 Responses of fixed-wing flight in the nominal case

quad-plane is commanded to follow the path at a constant airspeed (15 m/s). Meanwhile, the desired altitude of the path is 100 m.

The initial values of the quad-plane are trimmed values at the airspeed of 15 m/s and the altitude of 90 m. The overall path-following performance is shown in Figure 8. It can be seen that both control laws ensure effective path following of the quad-plane in the nominal case, although the altitude response has a relatively large overshoot using the ADRC+PID control law.

The detailed outer loop, Euler angle, and actuator responses in the nominal case are presented in Figure 9. It can be seen that the commands for altitude, airspeed, course angle, and sideslip angle are well tracked by both control laws. Initially, there is an overshoot in the altitude response. The overshoot based on the INDI control law is 10%, whereas the overshoot based on the ADRC+PID control law is 24%. Also, there is only a slight coupling between airspeed and altitude with the INDI control law, but it is much larger with the ADRC+PID control law. In addition, the sideslip angle has a certain coupling with the course angle, but the oscillation amplitude is less than 2° and can be reduced to zero faster using the INDI control law. The corresponding pitch and roll angles are within the range of [−30°, 30°], which is an attitude range suitable for quad-plane flight missions such as transporting cargo. During the turn, the roll angle value

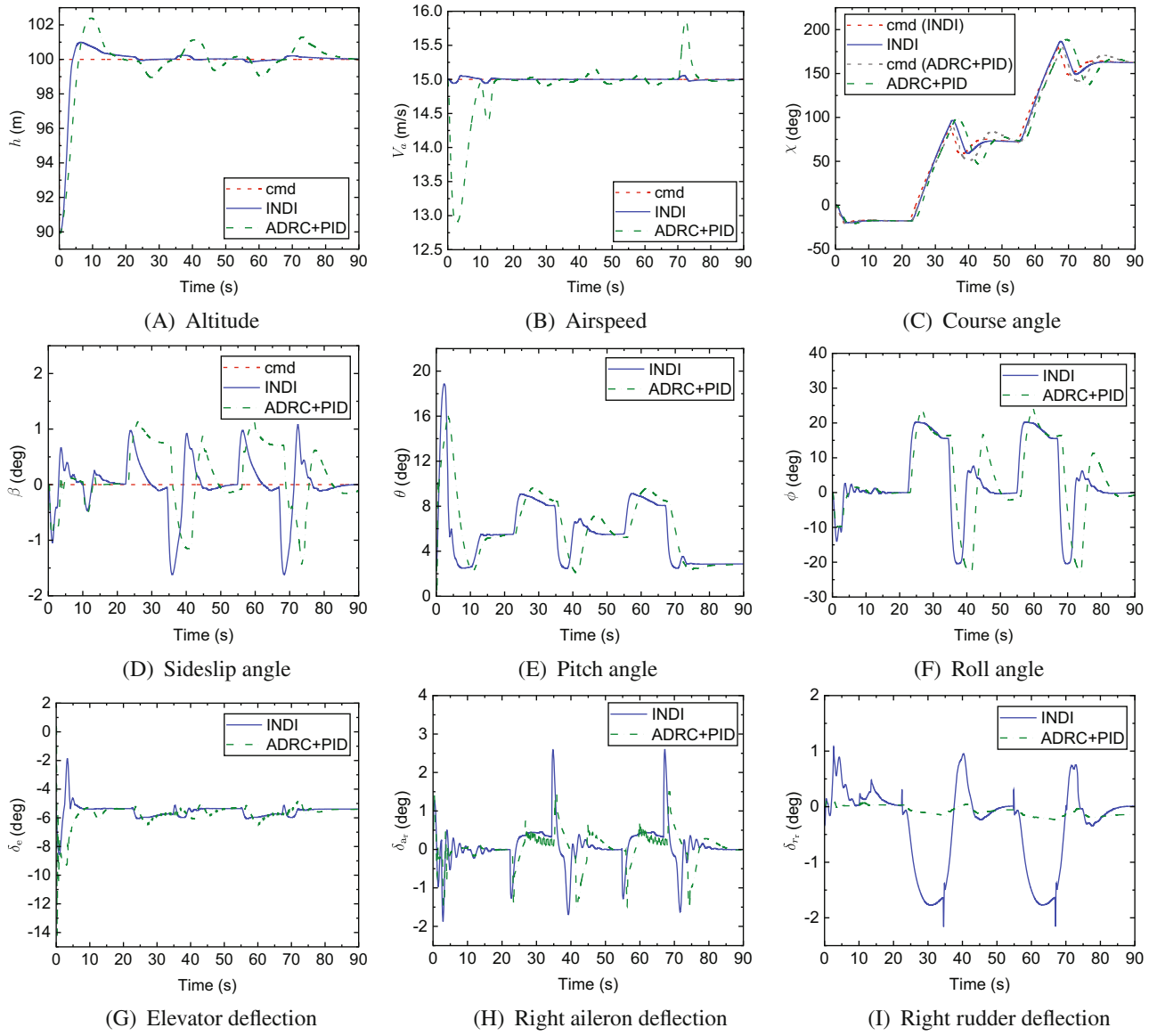

FIGURE 10 Responses of fixed-wing flight in the wind gust disturbance case

greatly varies, which is the effect of the coordinated turn. The elevator, right aileron, and right rudder responses do not exceed their ranges of $[-21°, 21°]$, $[-31°, 31°]$, and $[-29°, 29°]$, respectively.

6.1.2 | Wind gust disturbance case

In the flight of UAVs, they often face interference from wind gusts. Therefore, it is necessary to observe the response characteristics of UAVs under wind gust disturbances. The wind gust disturbance in this simulation is generated by the discrete wind gust model block* in Simulink, and the gust amplitudes are 3, 3, and 1 m/s along x-, y-, and z-axes in the body frame, respectively. It begins at 10 s and ends at 70 s. The simulation results are shown in Figure 10. It can be found that the commands of altitude, airspeed, course angle, and sideslip angle can still be tracked well with INDI control law in the presence of wind gusts, and the roll angle, pitch angle, and actuator values are within the ranges of variation. However, with the ADRC+PID control law, the system response has a larger oscillation under wind gusts. After the wind gust ends, the system regains its nominal characteristics. It can be concluded that the quad-plane has better flight performance under wind gust disturbances by the INDI control law in fixed-wing flight.

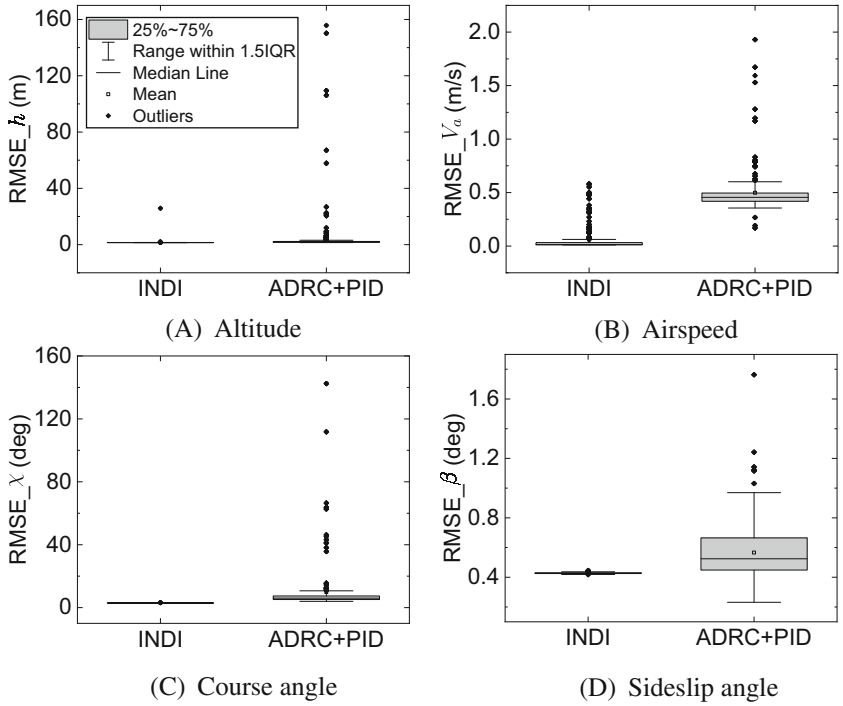

FIGURE 11 Box plots of RMSEs of outer tracking responses in fixed-wing flight

TABLE 8 Median and IQR values of RMSEs of outer tracking responses in fixed-wing flight

Method	Metrics	h (m)	V_a (m/s)	χ (deg)	β (deg)
INDI	Median	1.4540	0.0125	2.9423	0.4272
	IQR	0.0487	0.0202	0.1268	0.0048
ADRC+PID	Median	1.7973	0.4552	6.0427	0.5241
	IQR	0.5979	0.0772	2.2785	0.2167

6.1.3 | Model parameter uncertainty case

Model parameter uncertainties are hard to eliminate when building mathematical models, so the designed control law needs to be robust to model parameter uncertainties. In this subsection, Monte Carlo simulation experiments are conducted to verify the robustness of the two control laws.

The parameter uncertainties of the quad-plane model are assumed to follow normal distributions,[27] which yields

$$\Delta \sim \mathcal{N}(0, \sigma^2), \tag{49}$$

where the standard deviation σ is determined by the parameter measurement process. For this quad-plane model, the standard deviation of the mass uncertainty is chosen as 5% of the nominal mass. The standard deviations of the inertia parameter $(I_{xx}, I_{yy}, I_{zz}, I_{xz})$ uncertainties equal 15% of the nominal values. For the pusher propeller coefficient uncertainty, it is 20% of the nominal value. The standard deviations of the aerodynamic coefficient uncertainties are taken as 20% of the nominal values.

The reference signals in the simulation are the same as those in the nominal case, and the simulation with model uncertainties is repeated 1000 times using each of these two methods. The root mean square errors (RMSEs) of altitude, airspeed, course angle, and sideslip angle tracking responses are plotted as box plots presented in Figure 11, and the median and interquartile range (IQR) values of the RMSEs are listed in Table 8. It can be seen that the median and IQR values using both methods are small, demonstrating they are robust to model parameter uncertainties. However,

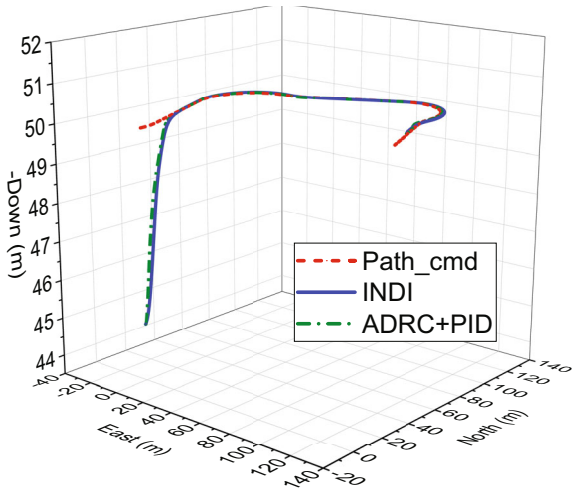

FIGURE 12 Path-following performance of hover flight in the nominal case

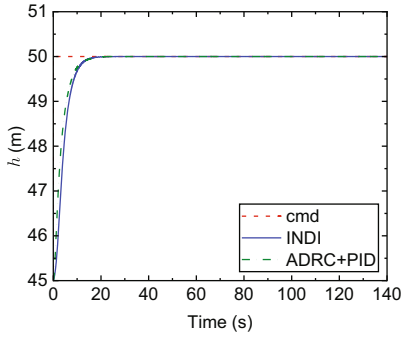

(A) Altitude

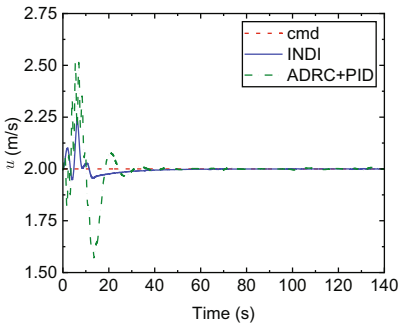

(B) Velocity u

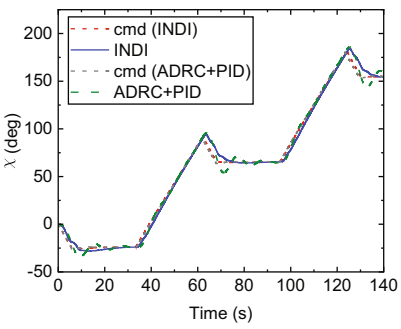

(C) Course angle

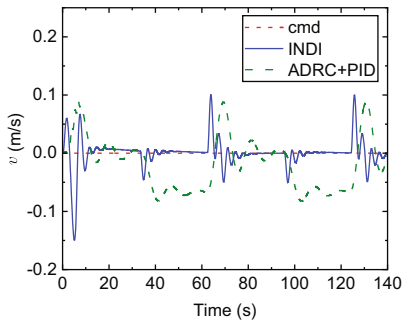

(D) Velocity v

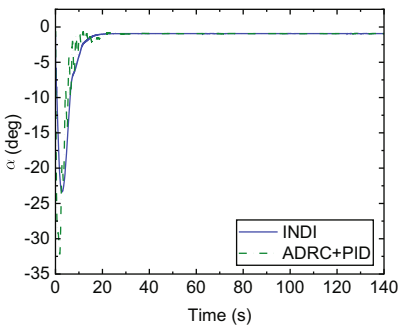

(E) Angle of attack

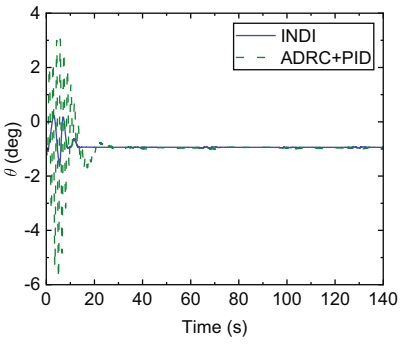

(F) Pitch angle

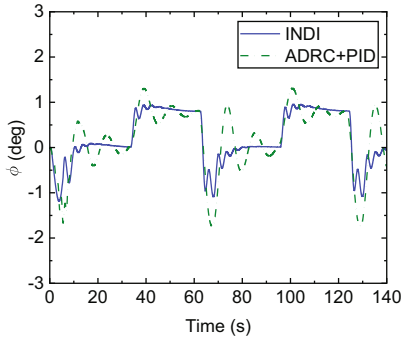

(G) Roll angle

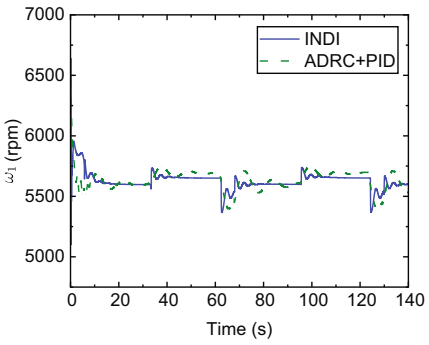

(H) Rotational speed of the lift motor 1

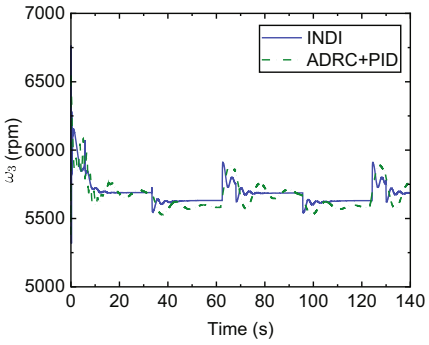

(I) Rotational speed of the lift motor 3

FIGURE 13 Responses of hover flight in the nominal case

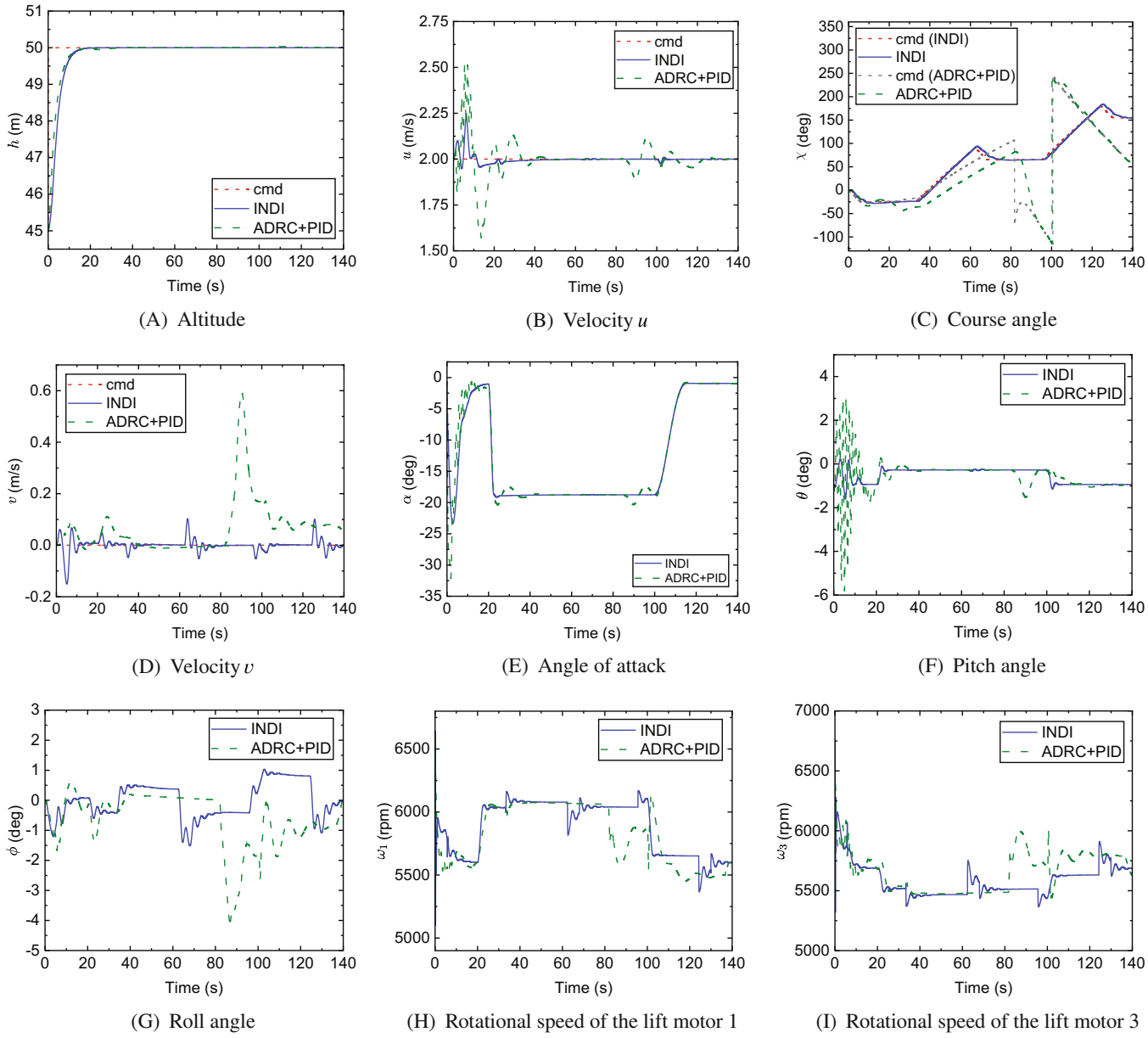

(A) Altitude (B) Velocity u (C) Course angle

(D) Velocity v (E) Angle of attack (F) Pitch angle

(G) Roll angle (H) Rotational speed of the lift motor 1 (I) Rotational speed of the lift motor 3

FIGURE 14 Responses of hover flight in the wind gust disturbance case

the values by the INDI control law are smaller than those by the ADRC+PID control law, and there are more and larger outliers using the ADRC+PID control law, which means that the system cannot track the reference commands accurately in many samples. In contrast, the INDI control law has better robustness in fixed-wing flight.

6.2 | Path following in hover flight

Similar to the fixed-wing simulation, three sets of simulation experiments are performed in hover flight: nominal case, wind gust disturbance case, and model parameter uncertainty case. Simulations of the control law designed based on ADRC and PID control methods are also conducted as a comparison group. For the hover flight control structure (see Figure 5), the control laws for pitch angle θ, roll angle ϕ, and course angle χ are designed by the ADRC method, whereas the control laws for velocity u, velocity v, and altitude h are based on PID controllers.

TABLE 9 Median and IQR values of RMSEs of outer tracking responses in hover flight

Method	Metrics	u (m/s)	h (m)	χ (deg)	v (m/s)
INDI	Median	0.3112	0.7162	4.2271	0.0262
	IQR	0.0119	0.0013	0.0203	0.0045
ADRC+PID	Median	0.1053	0.5985	5.3951	0.0495
	IQR	0.0537	0.0106	1.0684	0.0022

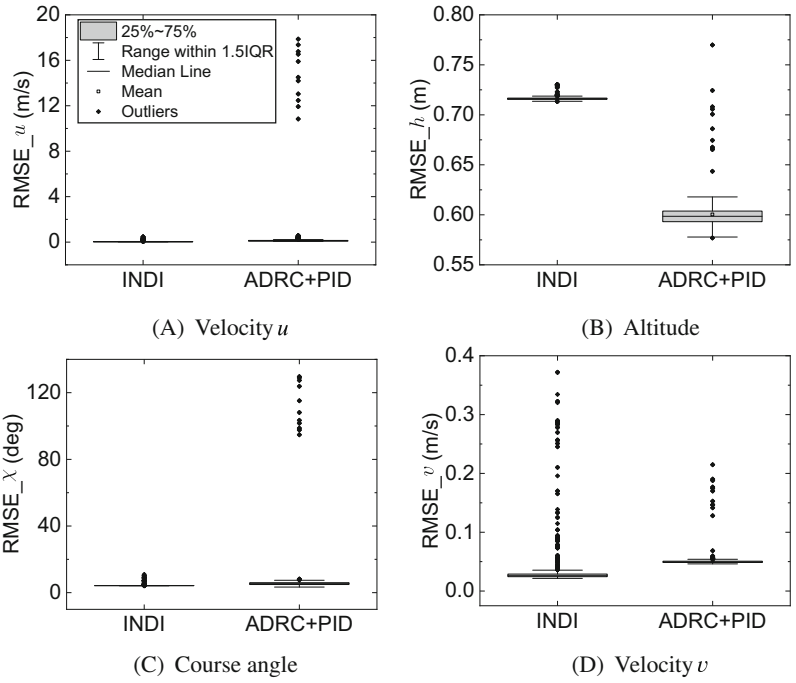

FIGURE 15 Box plots of RMSEs of outer tracking responses in hover flight

6.2.1 | Nominal case

In hover flight, the path-following objective is to follow a path (see Figure 12) with a constant velocity u (2 m/s). Additionally, the velocity v is set to be 0 m/s during hover flight to simplify the aerodynamics of the quad-plane. The model is firstly trimmed at the velocity u of 2 m/s and the altitude of 45 m. Figures 12 and 13 illustrate the overall path-following performance and detailed system response of hover flight in the nominal case, respectively. Both control laws enable the nominal quad-plane model to follow the path accurately, but the responses based on the ADRC+PID control law have more violent oscillations. The altitude command is tracked well. Meanwhile, the velocity u changes initially. The first reason is that it is coupled to the altitude h, and the second reason is that the angle of attack also changes when adjusting the altitude (see Figure 13E), generating some aerodynamic forces and moments due to the quad-plane hybrid structure, despite the low airspeed. But it can be held at 2 m/s after a short adjusting time. The course angle command is tracked well, while the velocity v can be held at 0 m/s and has a small oscillation amplitude of less than 0.2 m/s when the course angle changes drastically. The lift motors' rotational speeds are in the limited range of [0, 9356] rpm.

6.2.2 | Wind gust disturbance case

The wind gust disturbance in hover flight is also generated by the discrete wind gust model block in Simulink. The gust amplitudes are 0.5, 0.5, and 0.5 m/s along x-, y-, and z-axes in the body frame, respectively. The beginning is at 20 s, and the end is at 100 s. Simulation results are shown in Figure 14. It can be seen that the INDI control law can still enable

the quad-plane to track the commands well, just as in the nominal case. However, there is a large tracking error in the course angle response using the ADRC+PID control law, resulting in the quad-plane not following the circular path. There are also large oscillations in the responses using the ADRC+PID control law. Thus, the INDI control law can reject the disturbance better than the ADRC+PID control law in hover flight.

6.2.3 | Model parameter uncertainty case

Similar to the fixed-wing simulation, the Monte Carlo simulation is also performed to verify the robustness of the control law to model parameter uncertainties. In addition to the model uncertainties introduced in Section 6.1.3, uncertainties of the coefficients associated with lift motors are also considered in hover flight. They also follow normal distributions presented in Equation (49), and the standard deviations are 10% of the nominal values. The reference commands for the simulation are the same as those in the nominal case. 1000 simulations with model uncertainties are conducted using each of these two control laws. Box plots of RMSEs for the outer response tracking are presented in Figure 15, and the median and IQR values of the RMSEs are listed in Table 9. It can be seen that the median and IQR values with both methods are small in hover flight, which means they are robust to model parameter uncertainties, and most of the values with the INDI control law are similar to those with the ADRC+PID control law. However, there are extremely large outliers in the velocity u and course angle χ RMSEs by the ADRC+PID control law, indicating that the reference tracking of these samples is unsuccessful. In this case, the INDI control law has better robustness in hover flight.

7 | CONCLUSIONS

In this article, flight control laws based on INDI are designed for a quad-plane in fixed-wing and hover flight regimes to follow a given path. Firstly, a mathematical model of the quad-plane is illustrated on the basis of the kinematic and dynamic equations. Subsequently, cascade control structures are proposed, and control laws based on INDI are derived from the inner loop to the outer loop for fixed-wing and hover flight regimes. Finally, simulations are conducted to verify the performance and robustness of the designed control law. The control law based on ADRC and PID control methods is used as a comparison group. Simulation results indicate that the quad-plane can follow the path stably and accurately using the INDI control law, and it is more robust than the ADRC+PID control law. As quad-planes are novel and have few relevant studies, the research results of this article are significant supplements to the control law research for quad-planes. In future work, a control law for the transition flight regime will be designed, and other effective control methods will be utilized for the quad-plane. Flight tests will be carried out to evaluate the developed control laws.

ACKNOWLEDGMENTS

The authors would like to thank F. Prochazka and S. Krüger for their contributions during the construction and modeling of the quad-plane. This work was supported by the China Scholarship Council. Open Access funding enabled and organized by Projekt DEAL.

CONFLICT OF INTEREST

The authors declare no potential conflict of interests.

DATA AVAILABILITY STATEMENT

Data sharing is not applicable to this article as no datasets were generated or analyzed during the current study.

ENDNOTE

*https://www.mathworks.com/help/aeroblks/discretewindgustmodel.html#responsive_offcanvas

ORCID

Li Zhou https://orcid.org/0000-0001-6232-0227

REFERENCES

1. Ma'sum MA, Arrofi MK, Jati G, et al. Simulation of intelligent Unmanned Aerial Vehicle (UAV) For military surveillance. *International Conference on Advanced Computer Science and Information Systems (ICACSIS)*. Vol 2013. IEEE; 2013:161-166.
2. Nex F, Remondino F. UAV for 3D mapping applications: a review. *Appl Geomat*. 2014;6(1):1-15.
3. Radoglou-Grammatikis P, Sarigiannidis P, Lagkas T, Moscholios I. A compilation of UAV applications for precision agriculture. *Comput Netw*. 2020;172:107148.
4. Chen AY, Huang YN, Han JY, Kang SCJ. A review of rotorcraft unmanned aerial vehicle (UAV) developments and applications in civil engineering. *Smart Struct Syst*. 2014;13(6):1065-1094.
5. Saeed AS, Younes AB, Cai C, Cai G. A survey of hybrid unmanned aerial vehicles. *Prog Aerosp Sci*. 2018;98:91-105.
6. Chen C, Zhang J, Zhang D, Shen L. Control and flight test of a tilt-rotor unmanned aerial vehicle. *Int J Adv Robot Syst*. 2017;14(1):1729881416678141.
7. Flores-Colunga GR, Lozano-Leal R. A nonlinear control law for hover to level flight for the quad tilt-rotor uav. *The International Federation of Automatic Control*. Vol 2014. Elsevier; 2014:11055-11059.
8. Papachristos C, Tzes A. Modeling and control simulation of an unmanned tilt tri-rotor aerial vehicle. *IEEE International Conference on Industrial Technology*. Vol 2012. IEEE; 2012:840-845.
9. Yildiz Y, Unel M, Demirel AE. Nonlinear hierarchical control of a quad tilt-wing UAV: An adaptive control approach. *Int J Adapt Control Signal Process*. 2017;31(9):1245-1264.
10. Wang Y, Zhou Y, Lin C. Modeling and control for the mode transition of a novel tilt-wing UAV. *Aerosp Sci Technol*. 2019;91:593-606.
11. Yildiz Y, Unel M, Demirel AE. Adaptive nonlinear hierarchical control of a quad tilt-wing UAV. *European Control Conference (ECC)*. Vol 2015. IEEE.; 2015:3623-3628.
12. Yang Y, Yang J, Wang X, Zhu J. Robust optimal transition maneuvers control for tail-sitter unmanned aerial vehicles. *Int J Robust Nonlinear Control*. 2021;31(16):8007-8029.
13. Verling S, Weibel B, Boosfeld M, Alexis K, Burri M, Siegwart R. Full attitude control of a VTOL tailsitter UAV. *IEEE international conference on robotics and automation (ICRA)*. Vol 2016. IEEE; 2016:3006-3012.
14. Zhou W, Li B, Sun J, Wen CY, Chen CK. Position control of a tail-sitter UAV using successive linearization based model predictive control. *Control Eng Pract*. 2019;91:104125.
15. Çakici F, Leblebicioğlu MK. Control system design of a vertical take-off and landing fixed-wing UAV. *IFAC-papersonline*. 2016;49(3):267-272.
16. Dewi PT, Hadi GS, Kusnaedi MR, Budiyarto A, Budiyono A. Design of separate lift and thrust hybrid unmanned aerial vehicle. *J Instrum Automation Syst*. 2015;2(2):45-51.
17. Hadi GS, Kusnaedi MR, Dewi P, Budiyarto A, Budiyono A. Design of avionics system and control scenario of small hybrid vertical take-Off and landing (VTOL) UAV. *J Instrum Automation Syst*. 2015;2(2):67-71.
18. Hadi GS, Putra HM, Dewi PT, Budiyarto A, Budiyono A. Switching Control Approach for Stable Transition State Process on Hybrid Vertical Take-off and Landing UAV. *J Unmanned Syst Technol*. 2016;4(2):51-56.
19. Gu H, Lyu X, Li Z, Shen S, Zhang F. Development and experimental verification of a hybrid vertical take-off and landing (VTOL) unmanned aerial vehicle (UAV). *International Conference on Unmanned Aircraft Systems (ICUAS)*. Vol 2017. IEEE; 2017:160-169.
20. Zhang J, Guo Z, Wu L. Research on control scheme of vertical take-off and landing fixed-wing UAV. *2nd Asia-Pacific Conference on Intelligent Robot Systems (ACIRS)*. Vol 2017. IEEE; 2017:200-204.
21. Lin K, Qi J, Wu C, Wang M, Zhu G. Control System Design of A Vertical Take-off and Landing Unmanned Aerial Vehicle. *39th Chinese Control Conference (CCC)*. Vol 2020. IEEE; 2020:6750-6755.
22. Hanel M, Haimerl M, Bienert T. *Flight control laws for the quadcruiser RPA*. Deutsche Gesellschaft für Luft-und Raumfahrt-Lilienthal-Oberth eV; 2018.
23. Smith P. A simplified approach to nonlinear dynamic inversion based flight control. *23rd Atmospheric Flight Mechanics Conference*. AIAA; 1998:4461.
24. Bacon B, Ostroff A. Reconfigurable flight control using nonlinear dynamic inversion with a special accelerometer implementation. *AIAA Guidance, Navigation, and Control Conference and Exhibit*. AIAA; 2000:4565.
25. Khalil H. *Nonlinear Systems*. Prentice Hall; 2002.
26. Veld vR, Van Kampen EJ, Chu QP. Stability and robustness analysis and improvements for incremental nonlinear dynamic inversion control. *AIAA Guidance, Navigation, and Control Conference*. Vol 2018. AIAA; 2018:1127.
27. Wang X, Van Kampen EJ, Chu Q, Lu P. Stability analysis for incremental nonlinear dynamic inversion control. *J Guid Control Dynam*. 2019;42(5):1116-1129.
28. Smeur EJ, Chu Q. Croon dGC. Adaptive incremental nonlinear dynamic inversion for attitude control of micro air vehicles. *J Guid Control Dynam*. 2016;39(3):450-461.
29. Smeur EJ, Bronz M. Croon dGC. Incremental control and guidance of hybrid aircraft applied to a tailsitter unmanned air vehicle. *J Guid Control Dynam*. 2020;43(2):274-287.
30. Raab SA, Zhang J, Bhardwaj P, Holzapfel F. Proposal of a unified control strategy for vertical take-off and landing transition aircraft configurations. *Applied Aerodynamics Conference*. Vol 2018. AIAA; 2018:3478.
31. Lombaerts T, Kaneshige J, Schuet S, Aponso BL, Shish KH, Hardy G. Dynamic inversion based full envelope flight control for an eVTOL vehicle using a unified framework. *AIAA Scitech 2020 Forum*. AIAA; 2020:1619.

32. Chen G, Liu A, Hu J, Feng J, Ma Z. Attitude and Altitude Control of Unmanned Aerial-Underwater Vehicle Based on Incremental Nonlinear Dynamic Inversion. *IEEE Access*. 2020;8:156129-156138.
33. Lu P, vEJ K, Visser dC, Chu Q. Aircraft fault-tolerant trajectory control using Incremental Nonlinear Dynamic Inversion. *Control Eng Pract.* 2016;57:126-141.
34. Karssies HJ, De Wagter C. Extended incremental non-linear control allocation (XINCA) for quadplanes. *Int J Micro Air Veh*. 2022;14:1-11.
35. Han J. From PID to active disturbance rejection control. *IEEE Trans Ind Electron*. 2009;56(3):900-906.
36. Sun H, Sun Q, Wu W, Chen Z, Tao J. Altitude control for flexible wing unmanned aerial vehicle based on active disturbance rejection control and feedforward compensation. *Int J Robust Nonlinear Control*. 2020;30(1):222-245.
37. Wang Q, Xiong H, Qiu B. *The Attitude Control of Transmission Line Fault Inspection UAV Based on ADRC*. 2017 International Conference on Industrial Informatics - Computing Technology, Intelligent Technology, Industrial Information Integration (ICIICII); 2017:186-189.
38. Beard RW, McLain TW. *Small unmanned aircraft*. Princeton University Press; 2012.
39. Prochazka F, Krüger S, Ribnitykz D. *Aerodynamic parameter identification of a hybrid unmanned aerial vehicle by using wind tunnel and free flight tests*. Deutscher Luft- und Raumfahrtkongress; 2020.
40. Stevens BL, Lewis FL, Johnson EN. *Aircraft control and simulation: dynamics, controls design, and autonomous systems*. John Wiley & Sons; 2015.
41. Quan Q. *Introduction to multicopter design and control*. Springer; 2017.
42. Durham W, Bordignon KA, Beck R. *Aircraft control allocation*. John Wiley & Sons; 2017.
43. Golub GH, Van Loan CF. *Matrix computations*. JHU press; 2013.
44. Bhardwaj P, Raab SA, Zhang J, Holzapfel F. Integrated reference model for a tilt-rotor vertical take-off and landing transition UAV. *Applied Aerodynamics Conference*. Vol 2018. AIAA; 2018:3479.
45. Ang KH, Chong G, Li Y. PID control system analysis, design, and technology. *IEEE Trans Control Syst Technol*. 2005;13(4):559-576.
46. Rubi B, Pérez R, Morcego B. A survey of path following control strategies for UAVs focused on quadrotors. *J Intell Robot Syst*. 2020;98(2):241-265.

How to cite this article: Zhou L, Yang J, Strampe T, Klingauf U. Incremental nonlinear dynamic inversion based path-following control for a hybrid quad-plane unmanned aerial vehicle. *Int J Robust Nonlinear Control*. 2023;33(17):10304-10327. doi: 10.1002/rnc.6503